Accepted for publication in ApJ, 2011 Nov 28
Preprint typeset using LaTeX style emulateapj v. 11/10/09

arXiv:1105.2824v2 [astro-ph.CO] 2 Dec 2011

AVERAGE METALLICITY AND STAR FORMATION RATE OF LYα EMITTERS PROBED BY A TRIPLE NARROW-BAND SURVEY †

Kimihiko Nakajima [1,3], Masami Ouchi [2,3,4,13], Kazuhiro Shimasaku [1,5], Yoshiaki Ono [1], Janice C. Lee [4,13], Sebastien Foucaud [6], Chun Ly [4,7,8,14], Daniel A. Dale [9], Samir Salim [10], Rose Finn [11], Omar Almaini [12], and Sadanori Okamura [1,5]

Accepted for publication in ApJ, 2011 Nov 28

ABSTRACT

We present the average metallicity and star-formation rate of Lyα emitters (LAEs) measured from our large-area survey with three narrow-band (NB) filters covering the Lyα, [O II]λ3727, and Hα+[N II] lines of LAEs at $z = 2.2$. We select 919 $z = 2.2$ LAEs from Subaru/Suprime-Cam NB data in conjunction with Magellan/IMACS spectroscopy. Of these LAEs, 561 and 105 are observed with KPNO/NEWFIRM near-infrared NB filters whose central wavelengths are matched to redshifted [O II] and Hα nebular lines, respectively. By stacking the near-infrared images of the LAEs, we successfully obtain average nebular-line fluxes of LAEs, the majority of which are too faint to be identified individually by narrow-band imaging or deep spectroscopy. The stacked object has an Hα luminosity of $1.7 \times 10^{42}\,\mathrm{erg\,s^{-1}}$ corresponding to a star formation rate (SFR) of $14\,M_\odot\,\mathrm{yr}^{-1}$. We place, for the first time, a firm lower limit to the average metallicity of LAEs of $Z \gtrsim 0.09\,Z_\odot$ (2σ) based on the [O II]/(Hα+[N II]) index together with photo-ionization models and empirical relations. This lower limit of metallicity rules out the hypothesis that LAEs, so far observed at $z \sim 2$, are extremely metal poor ($Z < 2 \times 10^{-2}\,Z_\odot$) galaxies at the 4σ level. This limit is higher than a simple extrapolation of the observed mass-metallicity relation of $z \sim 2$ UV-selected galaxies toward lower masses ($5 \times 10^8\,M_\odot$), but roughly consistent with a recently proposed fundamental mass-metallicity relation when the LAEs' relatively low SFR is taken into account. The Hα and Lyα luminosities of our NB-selected LAEs indicate that the escape fraction of Lyα photons is $\sim 12-30\,\%$, much higher than the values derived for other galaxy populations at $z \sim 2$.

Subject headings: galaxies: abundances — galaxies: evolution — galaxies: formation — galaxies: high-redshift — galaxies: star formation

1. INTRODUCTION

Galaxy mass is thought to be a fundamental quantity which governs the evolution of galaxies. Detailed observations of present-day galaxies show that various properties of galaxies such as star formation rate (SFR) and gas phase metallicity correlate with mass (e.g., Brinchmann et al. 2004; Tremonti et al. 2004; Ellison et al. 2008). Theoretically, galaxy formation models based on ΛCDM cosmology predict that galaxies grow through subsequent mergings of lower-mass objects and that galaxy properties are largely determined by their masses through mass-dependent processes at work in the evolution of galaxies (e.g., Blumenthal et al. 1984; Davis et al. 1985; Bardeen et al. 1986). Therefore, observations of the mass-dependence of galaxy properties back in cosmic time are crucial to understanding how galaxies evolve to acquire present-day properties.

Past observations have revealed that some physical quantities like SFR and metallicity correlate with mass also at high-z, although the correlation seems to evolve with redshift relative to the local galaxies (e.g., Reddy et al. 2006; Hayashi et al. 2009; Erb et al. 2006a; Maiolino et al. 2008; Mannucci et al. 2009). They demonstrated the importance of mass-dependent effects on galaxy evolution. However, high-z samples are biased for high-mass galaxies ($\gtrsim 10^9\,M_\odot$) because most of them are based on continuum selected samples, such as Lyman-break galaxies (LBGs; e.g., Steidel & Hamilton 1992) and BzK galaxies (e.g., Daddi et al. 2004).

Lyα emitters (LAEs), galaxies commonly observed at high redshifts with strong Lyα emission, are likely to be low-mass, young galaxies as suggested from their

---

nakajima@astron.s.u-tokyo.ac.jp
[1] Department of Astronomy, Graduate School of Science, The University of Tokyo, 7-3-1 Hongo, Bunkyo-ku, Tokyo 113-0033, Japan
[2] Institute for Cosmic Ray Research, The University of Tokyo, 5-1-5 Kashiwanoha, Kashiwa, Chiba 277-8582, Japan
[3] Institute for the Physics and Mathematics of the Universe (IPMU), TODIAS, The University of Tokyo, 5-1-5 Kashiwanoha, Kashiwa, Chiba 277-8583, Japan
[4] Observatories of the Carnegie Institution of Washington, 813 Santa Barbara Street, Pasadena, CA 91101, USA
[5] Research Center for the Early Universe, Graduate School of Science, The University of Tokyo, Tokyo 113-0033, Japan
[6] Department of Earth Sciences, National Taiwan Normal University, N°88, Tingzhou Road, Sec. 4, Taipei 11677, Taiwan (R.O.C.)
[7] Department of Physics and Astronomy, UCLA, Los Angeles, CA, USA
[8] Space Telescope Science Institute, Baltimore, MD, USA
[9] Department of Physics and Astronomy, University of Wyoming, Laramie, WY, USA
[10] Department of Astronomy, Indiana University, Bloomington, IN, USA
[11] Department of Physics, Siena College, Loudonville, NY, USA
[12] School of Physics & Astronomy, University of Nottingham, Nottingham, UK
[13] Carnegie Fellow
[14] Giacconi Fellow

† Based in part on data collected at Subaru Telescope, which is operated by the National Astronomical Observatory of Japan.

TABLE 1
Summary of NB387 Imaging Data in the SXDS field

Field Name	Exp. Time (1)	PSF (2)	Area (3)	$m_{\rm lim}$ (4)	Date
SXDS-C	3.20 [9]	0.88	587 [41]	25.7 [25.3]	2009 Dec 14 - 16
SXDS-N	2.50 [5]	0.70	409 [159]	25.6 [25.2]	2009 Dec 16
SXDS-S	2.50 [5]	0.85	775 [344]	25.7 [25.3]	2009 Dec 16
SXDS-E$^{(5)}$	3.33 [10]	1.95	···	···	2009 Dec 19, 20
SXDS-W	1.83 [5]	1.23	232 [122]	25.1 [24.7]	2009 Dec 16, 19

(1) Total exposure times (hour). The value in square brackets shows the numbers of exposures that are combined.

(2) FWHM of PSFs of the stacked image that are registered with broadband images (arcsec).

(3) Effective area that is used for the selection (arcmin^2). The value in square brackets shows the area with low-S/N.

(4) Limiting magnitude derived from 5σ sky noise in a $2''$ diameter aperture. Note that $m_{\rm lim}$ in the SXDS-W is defined in a $2.''5$ diameter aperture. The magnitude in square brackets shows the limiting magnitudes in the low-S/N regions.

(5) The SXDS-E has large PSF size and is not included in the following analysis. So, we do not report the $m_{\rm lim}$ and covered area in this field.

small sizes, faint continua, and low stellar masses inferred from spectral energy distribution (SED) fitting ($\lesssim 10^9\,M_\odot$; Gawiser et al. 2006, 2007; Finkelstein et al. 2007, 2008, 2009; Nilsson et al. 2007; Pirzkal et al. 2007; Lai et al. 2008; Ono et al. 2010a,b; Yuma et al. 2010). Since they can be efficiently detected by narrow-band imaging, LAEs are a useful probe to investigate low-mass galaxies in the early stages of galaxy evolution. Furthermore, low-mass galaxies at high redshifts such as LAEs are especially interesting since they are likely to be building blocks of massive galaxies seen in later epochs.

Thanks to the remarkable progress in observations of LAEs, our knowledge of their properties is rapidly accumulating (e.g., Cowie & Hu 1998; Malhotra & Rhoads 2002; Ouchi et al. 2003; Malhotra & Rhoads 2004; Gawiser et al. 2006; Kashikawa 2006; Shimasaku et al. 2006; Gronwall et al. 2007; Ouchi et al. 2008; Nilsson et al. 2009; Blanc et al. 2011; Guaita et al. 2010; Hayes et al. 2010; Ono et al. 2010a,b; Ouchi et al. 2010; Finkelstein et al. 2011; Guaita et al. 2011; Nilsson et al. 2011). However, in almost all the observations, physical properties of LAEs including SFR and metallicity have been generally estimated by the SED fitting of broadband photometry. This is in contrast to massive galaxies at similar redshifts. While a large number of massive, continuum-selected galaxies have now direct measurements of SFR and metallicity from nebular lines (e.g., Reddy et al. 2006; Erb et al. 2006b; Maiolino et al. 2008; Mannucci et al. 2009; Hayashi et al. 2009; Yoshikawa et al. 2010), there are only a few LAEs with such direct measurements (McLinden et al. 2011; Finkelstein et al. 2011). One of the major reasons for the paucity of the direct measurements is that well-studied LAEs are located at very high redshift ($3 < z < 7$), where (rest-frame optical) nebular lines redshift into infrared wavelengths that cannot be observed from the ground. However, nebular lines of bright LAEs at moderate redshifts ($z = 2-3$) have now been measured through recent LAE surveys (e.g., McLinden et al. 2011; Finkelstein et al. 2011). It is known that SFRs derived from SED fitting are dependent on the star formation history assumed, and they can vary by an order of magnitude among different histories (e.g., Ono et al. 2010a). It is also known that SED fitting cannot strongly constrain metallicities due to the degeneracy with age (e.g., Ono et al. 2010a). Observations of nebular lines for a large number of LAEs are essential to extending star formation rate and metallicity measurements toward low-mass galaxies below $\sim 10^9\,M_\odot$, so that the mass-dependencies of SFR and metallicity can be compared with their present-day homologue over a full mass range.

We are conducting an imaging survey of $z \simeq 2.2$ LAEs in several fields on the sky using three narrow-band filters described below. This redshift is unique because [O II]λ3727 and Hα lines fall into wavelength ranges where OH-airglow is very weak, thus enabling one to study SFRs and metallicities of LAEs using these lines from the ground. We developed a new narrow-band filter, NB387, with a central wavelength and FWHM of 3870 Å and 94 Å, respectively, to select LAEs over $z = 2.14-2.22$. [O II] and Hα lines in this redshift range are then observed through near-infrared (NIR) narrow-band filters, NB118 ($\lambda_c = 11866$ Å, FWHM$=$ 111 Å) and NB209 ($\lambda_c = 20958$ Å, FWHM$=$ 205 Å), respectively, developed by the NewHα Survey (Lee et al. in preparation). In this paper, we present the results from data of the Subaru/*XMM-Newton* Deep Survey field, which are the first results of this triple-narrowband survey.

While our NB118 and NB209 imaging in the SXDS is not deep enough to detect [O II] and Hα lines for individual objects except for very luminous ones, we successfully detect these emission lines in the stacked images of more than 100 LAEs. We then measure their fluxes to derive the SFR and metallicity, and place the constraints on the average SFR and metallicity of a typical LAE at $z = 2.2$ for the first time. We use these measurements to discuss the SFR and metallicity of low-mass ($< 10^9\,M_\odot$) galaxies at $z \sim 2$.

Since Lyα photons produced in a galaxy are expected to be easily absorbed by dust in the interstellar medium (ISM) of the galaxy during repeated resonant scatterings by neutral hydrogen gas, a puzzle is why LAEs have such strong Lyα emission. There are three possible answers to the puzzle. The first is that LAEs are primordial galaxies (e.g., Scannapieco et al. 2003). If population III stars are formed following a top-heavy initial mass function, hard UV photons would be radiated in a short time scale, and strong Lyα lines would be observed. In this case, LAEs are young, and extremely metal poor galaxies. This will be tested by the metallicity we estimate. The second is that the ISM has a clumpy geometry (e.g., Neufeld 1991), where the Lyα photons are scattered at the sur-

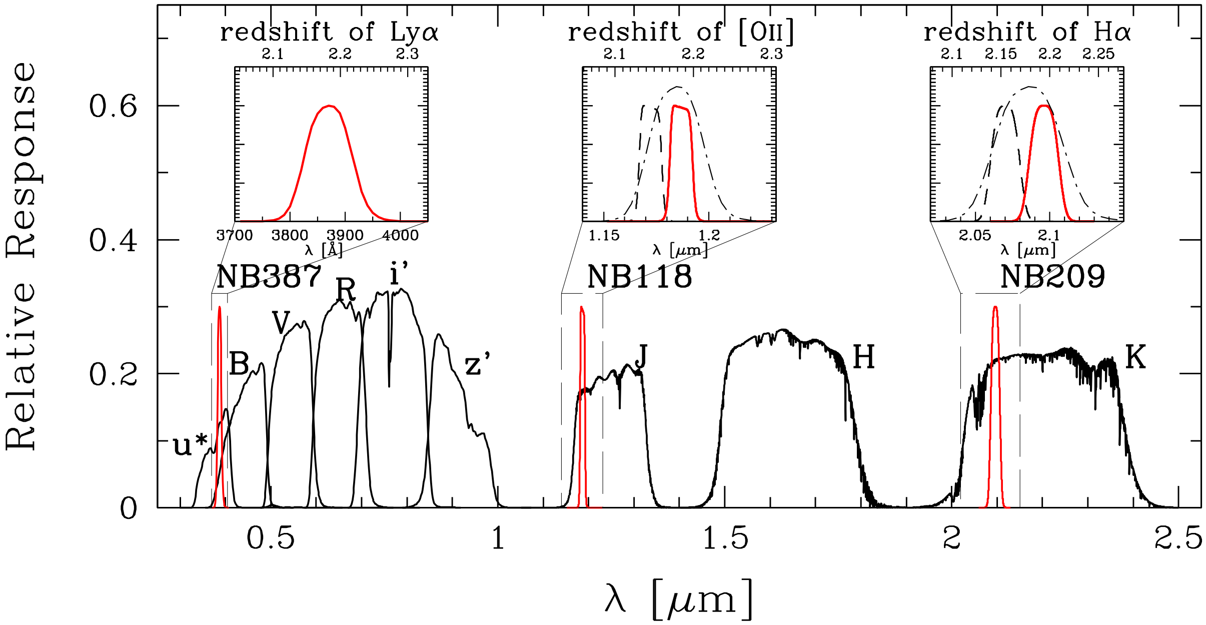

Fig. 1.— Relative response curves of the triple narrow-band filters, NB387 at Subaru and NB118 and NB209 at KPNO/NEWFIRM (red), superimposed on those of CFHT u^*, Subaru B, V, R, i', z', and UKIRT/WFCAM J, H, K (black). The responses include the throughputs of the instrument and the telescope as well as atmospheric absorption. The inner panels are a zoom in around NB387, NB118, and NB209, whose upper x-axis shows the redshift of Lyα, [O II], and Hα, respectively. In the NB118 and NB209 zoom-in panels, the dashed curves indicate the response curves of NB118 and NB209 at the corner of the filter (see text for details; Equation (1)), while the dot-dashed lines are re-scaled response curves of NB387 along the wavelength axis to sample [O II] and Hα after correction for a velocity offset between Lyα and nebular lines of $400\,\mathrm{km\,s^{-1}}$.

faces of the clumps and thus are not heavily absorbed before escaping from the galaxy. The third is the outflow of the ISM (e.g., Kunth et al. 1998). Lyα photons that are scattered at the far side of expanding ISM can be Doppler shifted to have redder wavelengths, and escape from galaxies without being heavily absorbed by neutral hydrogen gas. In order to investigate these possibilities, we estimate the Lyα escape fraction, $f_{\rm esc}^{\rm Ly\alpha}$, for our LAEs by comparing the observed Lyα luminosity with the intrinsic Lyα luminosity predicted from the dust-corrected Hα luminosity.

This paper is organized as follows. We describe the data in §2. The sample of $z = 2.2$ LAEs is constructed in §3, where the results of optical spectroscopy are also shown. In §4, we detect [O II] and Hα emission in the stacked LAEs and calculate their equivalent widths. Objects with individual detections of these lines are also briefly mentioned. Results of SED fitting of the stacked LAEs are briefly described in §5. In §6, we derive SFR, metallicity, and $f_{\rm esc}^{\rm Ly\alpha}$ for our LAEs, and discuss their implications. Conclusions are given in §7. Throughout this paper, magnitudes are given in the AB system (Oke 1974), and we assume a standard ΛCDM cosmology with $(\Omega_m, \Omega_\Lambda, H_0) = (0.3, 0.7, 70\,\mathrm{km\,s^{-1}\,Mpc^{-1}})$

2. IMAGING DATA

In this section we describe the optical and NIR data in the SXDS field used in our analysis.

2.1. *NB387 Images*

We carried out NB387 imaging observations of the SXDS with Subaru/Suprime-Cam (Miyazaki et al. 2002) on 2009 December 14-16 and 19-20. Table 1 summarizes the details of the observations. The SXDS field is covered by deep Suprime-Cam broadband data in five pointings with small overlaps; these five 'sub-fields' are named SXDS-C, -N, -S, -E, and -W, respectively, after their relative positions on the sky (Furusawa et al. 2008). We acquired NB387 imaging for all the five sub-fields (Table 1). We do not, however, use the data of SXDS-E in this study because of bad seeing. For photometric calibration, we observed spectrophotometric standard stars Feige34, LDS749B, and G93-48 (Oke 1990). Each standard star was observed more than twice under photometric condition with airmasses of $1.1 - 1.3$.

We used the Suprime-Cam Deep Field Reduction package (SDFRED; Yagi et al. 2002; Ouchi et al. 2004) to reduce the NB387 data. The data reduction process included bias subtraction, flat fielding, distortion correction, cosmic ray rejection, sky subtraction, bad pixel/satellite trail masking, image shifting, and stacking. For cosmic ray rejection, we used *LA.COSMIC* (van Dokkum 2001). After the stacking process, our images were registered with the archival broadband images (§2.2) using bright stellar objects commonly detected in the NB387 and the broadband images.

The PSF sizes of the registered images for the four sub-fields are $0''.70 - 1''.2$. The 5σ detection limits in a $2''$ diameter aperture are $25.1 - 25.7$ mag except on the edges of the images where signal-to-noise ratios (S/N) were significantly lower due to dithering. However, we include those low S/N regions to increase the number of LAEs, setting brighter limiting magnitudes according to the S/N ratios. The limiting magnitudes are estimated in the same manner as in Furusawa et al. (2008); we spread $5,000$ $2''.0$ diameter apertures over the entire image randomly after masking detected objects, and measure their photon counts. We then fit the negative

TABLE 2
Summary of Optical Broadband Imaging Data in the SXDS field

Band	Observatory	Field Name	PSF (1)	$m_{\rm lim}$ (2)	Reference (3)
$u^{*(4)}$	CFHT	SXDS-C,N,S,E,W	0.85	26.9	(a)
B	Subaru	SXDS-C,N,S,E,W	0.78 – 0.84	27.5 – 27.8	(b)
V	Subaru	SXDS-C,N,S,E,W	0.72 – 0.82	27.1 – 27.2	(b)
R	Subaru	SXDS-C,N,S,E,W	0.74 – 0.82	27.0 – 27.2	(b)
i'	Subaru	SXDS-C,N,S,E,W	0.68 – 0.82	26.9 – 27.1	(b)
z'	Subaru	SXDS-C,N,S,E,W	0.70 – 0.76	25.8 – 26.1	(b)

(1) PSF size is defined as a FWHM of point sources (arcsec).
(2) The limiting magnitude (5σ) estimated by 2″ diameter random aperture photometry.
(3) (a) Foucaud et al. in preparation, (b) Furusawa et al. (2008)
(4) The u^* image covers the same area of the UKIDSS/UDS project (Lawrence et al. 2007) which corresponds to about 77 % of the SXDS-C,-N,-S,-E, and -W.

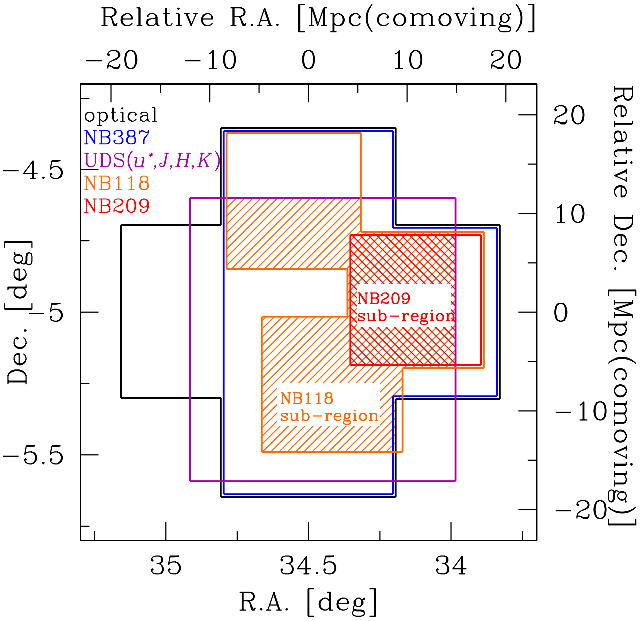

Fig. 2.— Areas covered by respective imaging data in the SXDS. Lines in different colors outline areas covered in different passbands: blue: NB387; magenta: u^* and J, H, K; orange: NB118; red: NB209; black: optical (B, V, R, i', z'). The orange-shaded and red-shaded regions correspond to the NB118 sub-region and the NB209 sub-region, respectively. Note that the NB209 sub-region is embedded in the the NB118 sub-region (see §3).

part of the histogram of the counts with Gaussian, and regard its σ as the 1σ sky fluctuations of the image for 2.″0 diameter apertures. The limiting magnitudes which appear in the following subsections are also estimated in the same manner.

We infer the errors in photometric zero points of our NB387 images from a comparison of colors (u^*-NB387 or $B-$NB387) of stellar objects in the images with those of 175 Galactic stars calculated from Gunn & Stryker (1983)'s spectrophotometric atlas. The estimated errors are less than 0.05 mag, which are small enough for our study.

2.2. *Optical Broadband Images*

The optical broadband data are required not only for selecting LAEs but also for performing SED fitting of the stacked object (Y. Ono et al. in preparation; briefly mentioned in §5). We use the publicly available B, V, R, i', and z' data taken with Subaru/Suprime-Cam by the SXDS project (Furusawa et al. 2008), and the u^* data taken with CFHT/MegaCam as part of the UKIDSS/UDS project (Foucaud et al. in preparation). Table 2 summarizes the details of the optical broadband data. The passbands of u^* and B, which are used to select LAEs as off-bands of NB387, are shown in Figure 1. We register the u^* image with the Suprime-Cam B image using common bright stars. The 5σ limiting magnitudes on a 2″ diameter aperture are: 26.9 (u^*), 27.5 − 27.8 (B), 27.1 − 27.2 (V), 27.0 − 27.2 (R), 26.9 − 27.1 (i'), 25.8 − 26.1 (z') mag. The u^* image covers 77 % of the Suprime-Cam field, nearly the same area as that of the UKIDSS/UDS JHK images (Lawrence et al. 2007; see §2.4) Figure 2 illustrates the sky coverages of our NB387 imaging, the Suprime-Cam broadband imaging, and the u^* imaging.

For each sub-field, PSF sizes were matched to the worst one among the $u^*BVRi'z'$ and NB387 images with the IRAF task `GAUSS`. The resulting PSF FWHMs of the images in the SXDS-C,N,S,W are 0.″88 (SXDS-C), 0.″85 (N), 0.″85 (S), and 1.″23 (W).

2.3. *NB118 and NB209 Images*

The SXDS field has been partly imaged in the NIR NB118 and NB209 narrowbands with KPNO/NEWFIRM by the NewHα Survey (Lee et al. in preparation). More details on the NB118 observations are given in Ly et al. (2011). The regions imaged are shown in Figure 2. The response curves of these two narrowband filters are shown in Figure 1 with those of the WFCAM J, H, and K bands (§2.4). Exposure times were 8.47 – 12.67 hr for NB118 and 11.75 hr for NB209. Both images were registered to the Suprime-Cam z' band images using common bright stars[16]. The 5σ limiting magnitudes in a 2″ diameter aperture are estimated to be $\simeq$ 23.6 mag for the NB118 and $\simeq$ 22.6 mag for the NB209 [17] . Errors in photometric zero points of the NB118 and NB209 images are less than 0.05 mag, which are inferred following the same manner as the NB387 images.

In NEWFIRM the incident angle to the filter surface is not exactly normal but varies as a function of the distance from the field center (Lee et al. in preparation;

---

[16] in order to run SExtractor in double-image mode (see §3.1).

[17] Our effective limiting magnitudes of NB118 and NB209 are 0.2 – 0.3 mag deeper than the magnitudes listed here owing to smoothing procedures (see §4.1). The limiting magnitudes after the smoothing are described in §4.2.

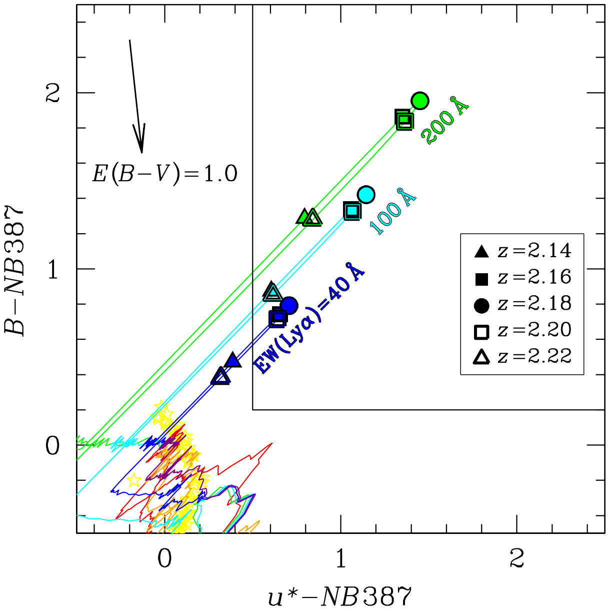

FIG. 3.— B−NB387 vs. u^*−NB387 plane for selection of LAEs at $z \simeq 2.2$. The solid lines in various colors indicate tracks of model galaxies redshifted from 0 to 3.5 with and without Lyα emission: purple: simple stellar population with an age of 0.03 Gyr; green, cyan, and blue: simple stellar population with Lyα emission of $\mathrm{EW_{rest}}$ = 200, 100, and 40 Å, respectively. The symbols on the tracks of model galaxies with Lyα emission correspond to z = 2.14 (filled triangles), 2.16 (filled squares), 2.18 (filled circles), 2.20 (open squares), and 2.22 (open triangles). The red and orange solid lines represent tracks of elliptical and spiral galaxies from the SWIRE template library (Polletta et al. 2007), respectively. The yellow stars show Galactic stars from Gunn & Stryker (1983). The tilted arrow indicates the reddening effect in the case of $E(B-V) = 1.0$ (Calzetti et al. 2000). The objects that are located in the area enclosed by the solid black lines are considered to be LAE candidates.

see also Tanaka et al. (2011) for Subaru/MOIRCS). Accordingly, the central wavelength of NB118 and NB209 also varies over the FoV, since both filters are interference filters. The central wavelength at an incident angle θ (angle from normal incidence) is given by

$$\lambda(\theta) = \lambda_0 \cos(\theta/n), \qquad (1)$$

where λ_0 is the wavelength at normal incidence and n is the index of refraction of the material on which interference film is coated. We adopt n = 1.50 for NB118 and n = 1.49 for NB209 (Lee et al. in preparation). At the corner of the filter θ has the maximum value of 13.5 degree. Thus, the maximum wavelength shifts are $\simeq -150$ Å and $\simeq -260$ Å for NB118 and NB209, respectively. The passband of NB387 is broad enough to cover Lyα lines at the redshifts of [O II] and Hα lines corresponding to these shifted wavelengths (see also inner panels of Figure 1). However, as seen in §4.1.2, we have to take into account the passband shift over the FoV when calculating the equivalent widths of [O II] and Hα lines of stacked objects.

2.4. *NIR Broadband Images*

The UKIDSS/UDS project provides deep J, H, and K images of UKIRT/WFCAM (Lawrence et al. 2007). In this paper, we use the data release 8 (DR8) images currently available to the UKIDSS consortium. The J and K images are used as off-bands of NB118 and NB209 to detect [O II] and Hα(+[N II]) emission, respectively, while the H image is used for SED fitting of the stacked objects. We register these three images with the Suprime-Cam z' band images in the same manner as for NB118 and NB209. The 5σ limiting magnitudes over a 2″ diameter aperture are estimated to be 24.8, 24.1, and 24.6 in the J, H, and K bands, respectively. J, H, and K response curves are shown in Figure 1.

3. PHOTOMETRIC SAMPLES OF LAES AT $Z = 2.2$

We select LAEs in a 2,003 arcmin^2 region which is covered by all the three passbands for selecting LAEs: NB387, u^*, and B (see Figure 2). In this paper, however, we use only LAEs in a sub-region of 1,283 arcmin^2 which is also covered by NB118. In this 'NB118 sub-region', a 353 arcmin^2 region is covered by NB209 as well ('NB209 sub-region'). Note that the J, H, K data are available for the NB118 sub-region. We use LAEs in the NB118 sub-region to derive the typical [O II] luminosity of LAEs, and those in the NB209 sub-region to derive the typical Hα luminosity of LAEs. The typical [O II] luminosity is also derived for LAEs in the NB209 sub-region to estimate the metallicity in combination with the Hα luminosity. In this section, we describe the construction of the LAE sample for the entire 2,003 arcmin^2 region.

3.1. *Object Detection and Candidate Selection*

We use the SExtractor software (Bertin & Arnouts 1996) to perform source detection and photometry. We run SExtractor in double-image mode, with the NB387 image used as the detection image. We identify sources with 5 adjoining pixels and brightness above $> 2\sigma$ of the sky background. The diameter to define aperture magnitudes is set to 2.″5 for the SXDS-W and 2.″0 for the other sub-fields. We use aperture magnitudes to calculate colors, and adopt `MAG_AUTO` for the total magnitude. All magnitudes are corrected for Galactic extinction of $E(B-V) = 0.020$ (Schlegel et al. 1998). The NB387-detection catalog contains 42,995 objects with aperture magnitudes brighter than the 5σ sky noise.

We select LAE candidates on the u^*−NB387 vs. B−NB387 color plane (Figure 3). In this figure, colors of model galaxies and Galactic stars are plotted in order to define the selection criteria for LAEs. The tracks indicate the colors of model galaxies redshifted from 0.00 to 3.50 with a step of $\Delta z = 0.01$. We assume the intergalactic medium (IGM) attenuation model of Madau (1995). Base on Figures 3 and 5, we define the color criteria of $z \sim 2.2$ LAEs as:

$$u^* - \mathrm{NB387} > 0.5 \;\&\&\; B - \mathrm{NB387} > 0.2, \qquad (2)$$

which select LAEs with $\mathrm{EW_{rest}} \gtrsim 30$ Å. The 2σ photometric errors in u^*−NB387 for the faintest objects (NB387=25.7) in our NB387-detected catalog are $\simeq 0.5$ mag. Thus, the criterion of u^*−NB387> 0.5 ensures that the contamination fraction in our LAE sample due to photometric errors is sufficiently low. We use 2σ limiting magnitudes instead when an object is not detected in u^* or B at 2σ level. The selection criteria require NB387 magnitude significantly brighter than both u^* and B magnitudes, which results in small number of non-emitters in the sample.

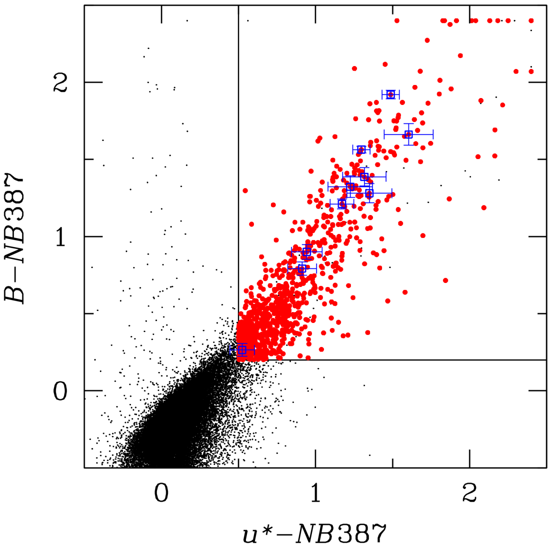

FIG. 4.— Distribution of NB387-detected objects in the $B-$NB387 vs. u^*-NB387 plane. The black dots indicate all the detected objects, while the red filled circles show LAE candidates after removing spurious objects and interlopers. The blue open squares with errorbars show spectroscopically confirmed LAEs. For the purpose of display, objects whose u^*-NB387 colors exceed 2.4 are plotted at u^*-NB387 = 2.4.

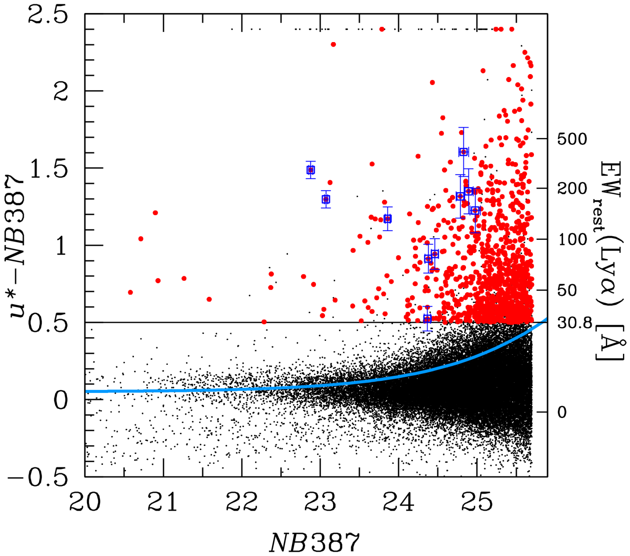

FIG. 5.— Distribution of NB387-detected objects in the u^*-NB387 vs. NB387 plane. The black dots indicate all the detected objects, while the red filled circles show LAE candidates. The blue open squares with errorbars show spectroscopically confirmed LAEs. For the purpose of display, objects whose u^*-NB387 colors exceed 2.4 are plotted at u^*-NB387= 2.4. The horizontal solid line shows the selection threshold of u^*-NB387 and the blue curve indicates the 2σ photometric error in u^*-NB387 for sources with u^*-NB387 = 0.05, which is the average u^*-NB387 color of all the objects. The right y axis shows the rest-frame Lyα equivalent width of $z = 2.18$ LAEs with u^*-NB387 color corresponding to the left y axis.

Using Equation (2), we identify $1,044$ LAE candidates in the NB387 detected catalog. These candidates are contaminated by spurious objects and foreground and background interlopers. We remove those contaminants by the procedures described in the next two subsections.

3.2. *Rejection of Spurious Objects*

Given the limited number of ditherings in our NB387 imaging ($\sim 4-5$), a clipped-mean stacking fails to completely remove the remaining cosmic rays which survived *LA.COSMIC* rejection on individual dithered images. Since cosmic rays have steeper light profiles than the PSF, we removed 21 sources with FWHMs significantly smaller than the PSF. We then perform visual inspection on all the remaining objects, and eliminate 90 obvious spurious sources such as ghosts due to bright stars and bad pixels.

3.3. *Identification of Interlopers*

In addition to LAEs, other emission line objects, such as [O II] emitters at $z \simeq 0.04$, Mg IIλ2798 emitters at $z \simeq 0.4$, and CIVλ1550 emitters at $z \simeq 1.5$, may be included in our sample. Our survey area, $2,003\,\mathrm{arcmin}^2$, corresponds to $400\,\mathrm{Mpc}^3$ for [O II] emitters, which is two orders of magnitude smaller than the volume sampled by Lyα emitters ($48,100\,\mathrm{Mpc}^3$). The number of [O II] emitters is therefore expected to be small.

To remove [O II] emitters from our sample, we use the Galaxy Evolution Explorer (GALEX) NUV (λ_c = 2267 Å, FWHM = 616 Å) and FUV (λ_c = 1516 Å, FWHM = 269 Å) data. Real LAEs in our sample will be invisible in these data, since these two passbands are located shortward of the Lyman break at $z \sim 2.2$. Thus, objects visible in either of the two GALEX band data are likely to be [O II] emitters. Although some studies have shown that ionizing photons are more likely to escape from Lyα selected galaxies than from UV-selected galaxies (e.g., Iwata 2009; Nestor et al. 2011), the estimated UV-to-Ly-continuum flux density ratio is $\gtrsim 2$ even for LAEs (Nestor et al. 2011), therefore the Ly-continuum of $z \sim 2$ LAEs is expected to be fainter than the UV continuum by ~ 1 mag or more. Since the detection limit of the GALEX images is ~ 24 (3σ) both in NUV and FUV, LAEs fainter than $V \sim 23$ should be invisible in the GALEX images. We find 12 objects which have a counterpart in either of the NUV or FUV image within $3''$ from the NB387 position. Among them, 4 are fainter than $V = 23$, thus to be inferred to be interlopers. The remaining eight are brighter than $V = 23$, and their GALEX magnitudes are also bright enough to be consistent with them being interlopers. Indeed, all eight are also detected as an X-ray or radio source as described in the next paragraph. We thus remove these 12 objects from the sample.

For Mg II and CIV emitters, we use X-ray and radio imaging data, since both emitters selected by Equation (2) should have large EWs ($\mathrm{EW_{rest}} \gtrsim 30$ Å) and thus they are likely to be AGNs. For X-ray data, we use the *XMM-Newton* $0.2-10.0$ keV band source catalog by Ueda et al. (2008). For radio data, we use the Very Large Array (VLA) 1.4 GHz source catalog by Simpson et al. (2006). After removing some confused objects by visual inspection, we find 11 (1) LAE candidates with an X-ray (radio) counterpart. The number

TABLE 3
PROPERTIES OF THE SPECTROSCOPIC SAMPLE

ID	R.A.$^{(1)}$	Dec.$^{(1)}$	mag(NB387) (2)	$\lambda_{\rm obs}$ (3)	z (4)	flag (5)
NB387-C-04640	02:18:48.968	-05:09:00.32	23.07 ± 0.02	3862.83	2.1767	b
NB387-C-07673	02:18:56.532	-05:05:48.41	24.98 ± 0.07	3853.55	2.1690	c
NB387-C-08099	02:19:05.729	-05:05:23.86	24.79 ± 0.05	3889.02	2.1982	c
NB387-C-08204	02:18:57.385	-05:05:18.82	24.46 ± 0.05	3895.63	2.2036	b
NB387-C-08321	02:19:05.279	-05:05:11.22	24.89 ± 0.06	3891.62	2.2003	b
NB387-C-09219	02:19:02.396	-05:04:19.27	24.37 ± 0.04	3890.03	2.1990	c
NB387-C-09951	02:18:50.038	-05:03:34.09	24.38 ± 0.04	3901.78	2.2087	b
NB387-C-11135	02:18:37.381	-05:02:24.61	23.86 ± 0.03	3882.13	2.1925	b
NB387-C-12596	02:18:55.071	-05:00:58.82	24.83 ± 0.06	3886.29	2.1960	c
NB387-C-16564	02:19:09.542	-04:57:13.32	22.88 ± 0.03	3861.44	2.1755	a

(1) Coordinates are in J2000.
(2) NB387 magnitudes with 2″ diameter apertures.
(3) Central wavelengths of observed Lyα lines (Å). We perform a Gaussian fitting to each detected line using MPFIT, and derive the central wavelengths.
(4) Redshifts of Lyα lines estimated from the central wavelengths.
(5) Flags of reliability of the lines by inspecting the 2D spectra by eye: "a" secure, "b" likely, "c" tentative.

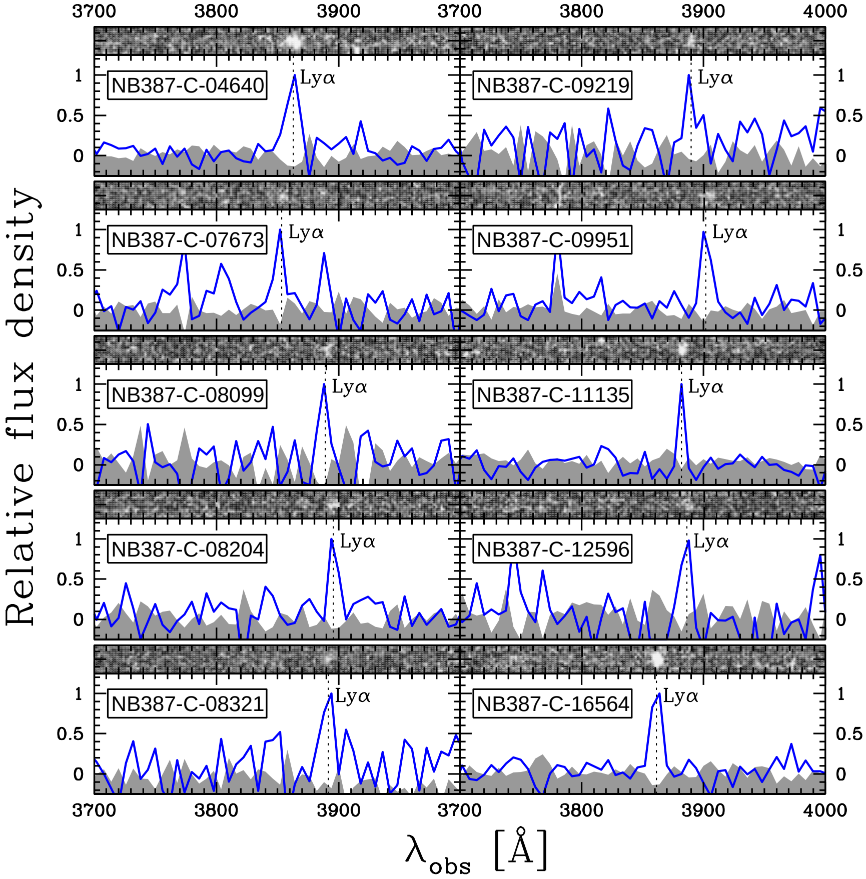

FIG. 6.— IMACS spectra of ten confirmed LAEs. For each object, the top panel shows the 2D spectrum, while the bottom panel showing the 1D spectrum (blue line) and the sky background (gray shaded area), both of which have been smoothed with a 3 pixel boxcar filter and arbitrarily normalized.

of likely Mg II or C IV emitters is thus 12. Note that 10 out of the 12 are also detected in the GALEX data.

After removing spurious objects and obvious [O II] and C IV emitters, we have 919 $(= 1,044 - (21 + 90) - (12 + 12 - 10))$ LAE candidates. Among them, 561 are in the NB118 sub-region and 105 in the NB209 sub-region. We plot all the candidates on the u^*-NB387 vs. $B-$NB387 two color plane in Figure 4 and on the u^*-NB387 vs. NB387 color-magnitude plane in Figure 5. Figure 3 and Figure 4 show that the candidates (red circles) are placed in the isolated region away from the locus of other galaxies and Galactic stars.

3.4. *Follow-up Spectroscopy Data*

We carried out follow-up spectroscopy of 30 objects selected from the whole sample ($N = 919$) so that they are distributed in wide ranges of NB387 magnitudes and

u^*-NB387 colors. The observations were made with the Inamori Magellan Areal Camera and Spectrograph (IMACS; Dressler et al. 2006) on the Magellan telescope using the 300 lines mm^{-1} grism and the WB3600 − 5700 filter on 2010 July 9-10 under photometric conditions. We used the $f/4$ camera, which has a better sensitivity than the $f/2$ camera at short wavelengths. The total throughput of the $f/4$ camera with the 300 lines mm^{-1} grism at 3870Å is 6.2 %, while that of the $f/2$ camera is 2.6 %. The on-source exposure time was 13, 700 seconds, with a seeing size of $0''.48 - 0''.63$. We chose a $0''.8$ slit width, which gives a resolving power of $R \sim 700$ around 4000 Å. The COSMOS pipeline was used for data reduction.

By inspecting the reduced spectra by eye, we detected an emission line around 3870 Å for ten objects, while the remaining 20 had no visible emission line. The main reason for this low detection rate is the bright limiting flux of our observation due to the low sensitivity below 4000 Å and the relatively short exposure time. Indeed, all ten objects with line emission are brighter than NB387 = 25.0, and the success rate limited to NB387 < 25.0 (13 objects in total) is found to be 10/13 = 77 %. Among the remaining three bright objects, two have NB387≃ 25.0 and may be marginally undetected. The other one object has NB387 = 24.4, but smaller Lyα flux expected from its u^*-NB387 compared with the confirmed candidates. The spectra of the ten confirmed LAEs are shown in Figure 6, and the NB387 magnitudes and Lyα-based redshifts are given in Table 3.

The ten objects are not [O II] emitters at $z \simeq 0.04$ because of the lack of [O III]λ5007 line at the corresponding wavelength, ≃ 5200 Å. They are not AGNs either, with Mg II emission at $z \simeq 0.4$ or CIV emission at $z \simeq 1.5$, because of the absence of emission lines at 3600 − 5700 Å (e.g., Mg II: [O II] line at ≃ 5150 Å, CIV: He IIλ1640 line at ≃ 4100 Å and C III]λ1909 line at ≃ 4770 Å) and because we have removed AGN candidates from the sample in advance (see §3.3). Therefore, we conclude that all ten objects are LAEs at $z \simeq 2.2$. This demonstrates that the contamination in our LAE sample is very low, at least for bright objects.

4. [O II] AND Hα EMISSION LINES

Our NIR images are not deep enough to study [O II] and Hα properties of LAEs based on individual detections. Indeed, only 10 objects have detection of [O II] emission and only 3 have detection of Hα+[N II] emission, as described in §4.2. We therefore carry out a stacking analysis of the whole LAE sample in the NB118 sub-region, and discuss average emission-line properties of $z \sim 2.2$ LAEs. The individually detected objects are discussed below and compared with the stacked objects.

4.1. *Stacking Analysis*

Stacking is done separately for the NB118 sub-region and the NB209 sub-region. For the NB118 sub-region, we stack the NB118 and J images at the positions of 561 LAE candidates. Similarly, for the NB209 sub-region, the NB118, J, NB209, and K images are stacked at the positions of the 105 LAE candidates. Before stacking, we mask regions affected by a ghost, a stellar halo, and bad pixels, as well as regions with relatively large noise. The stacked image in the NB118 sub-region are used to detect the [O II] flux at the highest S/N ratio, while the stacked image in the NB209 sub-region are used to compare [O II] and Hα fluxes in a common sample. To derive the average Lyα flux, we also stack NB387 and u^* images for each sub-region. All stackings are done by median-stacking. Before the stacking, we smooth the images with gaussian filters so that both narrowband and broadband images have the same PSF sizes. This enables us to measure the colors of the stacked objects by aperture photometry (§4.1.1). The PSF size before smoothing is $1''.6$ for NB118 and J, $1''.2$ for NB209 and K, and $1''.2$ for NB387 and u^*. We do not remove the individually detected objects from the stacking analysis in order to increase the number of candidates for stackings. In fact, results after removing the individually detected objects are consistent with the results in Equation (3) owing to the median-stacking.

The stacked NIR images are shown in Figure 7. A signal is clearly visible in all the passbands including NB118 and NB209. We measure the magnitudes and colors of the stacked images in §4.1.1, and convert them into line fluxes using Monte Carlo simulations in §4.1.2.

4.1.1. *Photometry*

We measure aperture magnitudes of the stacked objects using the IRAF task `phot`. The aperture diameter is set to be $2''.5 - 3''.2$ (about twice the PSF size) to calculate colors, while larger apertures of $4''.8 - 6''.1$ (depending on the passband) are adopted to obtain total magnitudes. Errors in the magnitudes are estimated in the same manner as in Ono et al. (2010b); we create 1, 000 median-stacked sky noise images, each of which is made of 561 (105) randomly-selected sky noise images in the NB118 (NB209) sub-regions. We then fit the negative part of histograms with a Gaussian, whose FWHMs are used to estimate the limiting magnitudes. The magnitudes and errors obtained are summarized in Table 4. The uncertainties of zero points are not included in the errors.

4.1.2. *Equivalent Widths and Fluxes of the Lines*

The $J-$NB118 and $K-$NB209 colors for the stacked objects are calculated to be:

$$\begin{aligned} J - \mathrm{NB118(NB118sub)} &= 0.43 \pm 0.05 \\ J - \mathrm{NB118(NB209sub)} &= 0.39 \pm 0.08, \\ K - \mathrm{NB209(NB209sub)} &= 0.65 \pm 0.11 \end{aligned} \tag{3}$$

where the color with 'NB118sub' and 'NB209sub' in round brackets is derived from the stacked object in the NB118 sub-region and that in the NB209 sub-region, respectively. These large, positive values with the small errors indicate significant detection of the lines. In order to estimate the [O II] and Hα+[N II] equivalent widths and fluxes with the best accuracy, we used Monte Carlo simulations. If both a narrowband and a broadband (which brackets the narrowband) filters have ideal top-hat response functions, an EW of an emission line falling in the narrowband can be calculated as:

$$\mathrm{EW_{rest}} = \frac{\left(f_\lambda^N - f_\lambda^B\right) \Delta\lambda^N \Delta\lambda^B}{\Delta\lambda^B f_\lambda^B - \Delta\lambda^N f_\lambda^N} \frac{1}{1+z}, \tag{4}$$

TABLE 4
Properties of the stacked LAEs in the two sub samples

sample $\cdots[N]^{(1)}$	Line	$m^B_{\rm aper}$ (2)	$m^N_{\rm aper}$ (3)	$m^N_{\rm total}$ (4)	EW$_{\rm rest}$ (5)	Flux (6)	Luminosity (7)
NB118 sub	[O II]	25.18 ± 0.02	24.74 ± 0.05	24.57	106^{+14}_{-12}	$9.65^{+0.39}_{-0.39} \times 10^{-18}$	$3.54^{+0.14}_{-0.14} \times 10^{41}$
$\cdots$ [561]	Lyα	25.83 ± 0.01	25.05 ± 0.01	24.87	86^{+3}_{-2}	$5.76^{+0.11}_{-0.09} \times 10^{-17}$	$2.11^{+0.04}_{-0.03} \times 10^{42}$
NB209 sub	[O II]	24.72 ± 0.03	24.33 ± 0.07	24.11	96^{+23}_{-19}	$1.44^{+0.09}_{-0.10} \times 10^{-17}$	$5.26^{+0.35}_{-0.38} \times 10^{41}$
$\cdots$ [105]	Hα+[N II]	24.72 ± 0.03	24.07 ± 0.10	23.62	271^{+242}_{-104}	$2.18^{+0.34}_{-0.33} \times 10^{-17}$	$7.98^{+1.25}_{-1.21} \times 10^{41}$
	H$\alpha^{(8)}$	$\cdots$	$\cdots$	$\cdots$	256^{+229}_{-98}	$2.06^{+0.32}_{-0.31} \times 10^{-17}$	$7.55^{+1.19}_{-1.15} \times 10^{41}$
	Lyα	25.75 ± 0.02	25.09 ± 0.02	24.94	63^{+3}_{-5}	$4.90^{+0.12}_{-0.19} \times 10^{-17}$	$1.80^{+0.05}_{-0.07} \times 10^{42}$

(1) Numbers of stacked objects in square brackets.

(2) Broadband aperture magnitudes and their 1σ errors. Broadbands are J for [O II], K for Hα+[N II], and u^* for Lyα. The diameter of the aperture is $2''\!.5 - 3''\!.2$. Aperture sizes are chosen to have twice the PSF sizes.

(3) Narrowband aperture magnitudes and their 1σ errors. Narrowbands are NB118 for [O II], NB209 for Hα+[N II], and NB387 for Lyα. The diameter of the aperture is $2''\!.5 - 3''\!.2$. Aperture sizes are chosen to have twice the PSF sizes.

(4) Narrowband total magnitudes. The diameters of the aperture are $4''\!.8$ and $6''\!.1$ for [O II] and Lyα line in the NB118 sub-region, respectively, and $5''\!.7$, $5''\!.7$, and $6''\!.1$ for [O II], Hα+[N II], and Lyα line in the NB209 sub-region, respectively. Aperture sizes are chosen to include close to 100 % of the flux.

(5) Rest-frame equivalent width of the lines (Å). For [O II] and Hα+[N II], EWs are estimated by Monte Carlo simulations (see §4.1.2 in details), and for Lyα, the colors of u^*-NB387 are used for the estimates of EWs.

(6) Line fluxes in unit of erg s^{-1} cm^{-2}.

(7) Line luminosities in unit of erg s^{-1}.

(8) The contribution from [N II]$\lambda\lambda$6584, 6548 lines is subtracted from the observed Hα+[N II] luminosity using the metallicity estimated in §6.2.1 (see also §6.1.1).

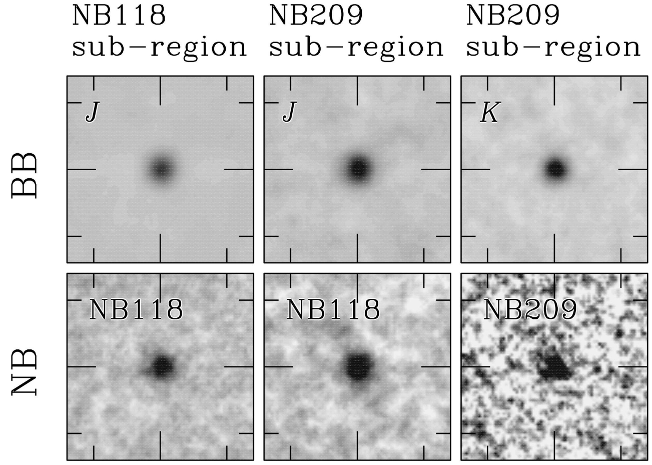

Fig. 7.— Snapshots of the stacked LAE in J (top left) and NB118 (bottom left) in the NB118 sub-region, and J (top center), NB118 (bottom center), K (top right), and NB209 (bottom right) in the NB209 sub-region. Each image is $15'' \times 15''$ in size.

where f_λ is the flux density per unit wavelength, $\Delta\lambda$ is the width of a given filter, z is redshift, and superscripts N and B indicate narrowband and broadband, respectively. To derive this formula, we have assumed that the flux density of the continuum emission is constant over the whole wavelength range. If this formula is used, the colors obtained above are converted into EW$_{\rm rest,NB118sub}$([O II])= 25 Å, EW$_{\rm rest,NB209sub}$([O II])= 23 Å, and EW$_{\rm rest,NB209sub}$(Hα+[N II])= 58 Å, respectively.

Although these values are useful as zero-order estimates, their accuracy is not sufficient for our purpose. In fact the assumption on the shape of the passband used to derive Equation (4) is over simplified in two aspects: the actual NB118 and NB209 passbands are not top-hat but rather close to a triangle shape and the central wavelengths of these passbands vary over the FoV (Equation (1); see §2.3). These issues must be considered to obtain correct EW values, since the objects used for stacking have different redshifts (corresponding to the different locations within the band width of NB387) and they are distributed across the FoV. In general, Equation (4) is correct only when a line is located where the response function of the narrowband peaks. In reality, however, a large fraction of the LAEs are expected to have [O II] and Hα+[N II] lines off the peak responses of NB118 and NB209 based on the re-scaled shapes of NB387 (see Figure 1). This means that the EWs of stacked objects calculated by Equation (4) are always underestimated.

We carry out Monte Carlo simulations taking into account of the above two points more accurately to estimate the EWs from the observed colors of the stacked objects. As an example, we describe below the simulations for the [O II] line of the objects in the NB118 subregion. The simulations for [O II] and Hα+[N II] lines in the NB209 sub-region are essentially the same.

The simulations are carried out under the assumption that all 561 objects have identical spectra, i.e., the same EW and the same underlying continuum spectra. For the continuum spectra, we use the best-fit spectrum from the SED fitting to the stacked LAE (see §5)[18]. We then vary EW$_{\rm rest}$ over −100 Å and 300 Å with 1 Å interval, and for each value we carry out a Monte Carlo simulation described by steps 1 − 4 below to derive the probability distribution of $J-$NB118 color for that EW. We thus simulate the relation between EW and $J-$NB118. The EW of the real, stacked object is calculated by substituting the observed $J-$NB118 color into the relation.

---

[18] We also try two independent SEDs for the simulation; the best-fit SED of spectroscopically confirmed BX galaxies at $2.0 < z < 2.2$ with constant star formation history (Guaita et al. 2011) and the best-fit spectrum from the SED fitting to the $z = 3.1$ stacked LAE (Ono et al. 2010a), and find that the results are consistent with each other well within their 1σ errors.

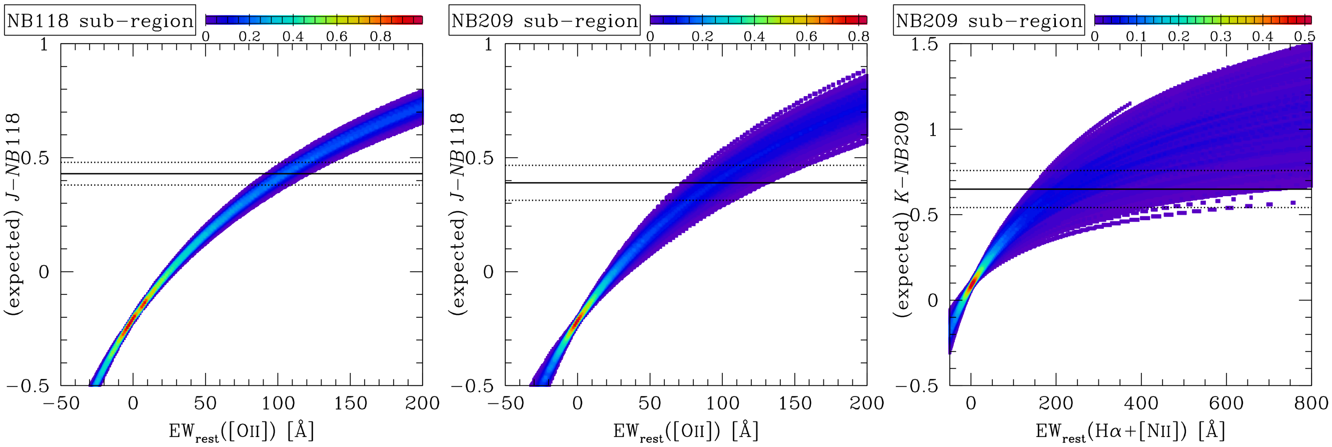

FIG. 8.— Relation between $\mathrm{EW_{rest}}$ and expected $J-$NB118 and $K-$NB209 colors from the Monte Carlo simulations: (left) $\mathrm{EW_{rest}}$([O II]) vs. $J-$NB118 in the NB118 sub-region; (center) $\mathrm{EW_{rest}}$([O II]) vs. $J-$NB118 in the NB209 sub-region; (right) $\mathrm{EW_{rest}}$(Hα+[N II]) vs. $K-$NB209 in the NB209 sub-region. The color contours indicate the probability of $J-$NB118 or $K-$NB209 at given $\mathrm{EW_{rest}}$; redder colors mean higher possibilities as shown in the color bars in the top. The solid black lines correspond to the measured $J-$NB118 or $K-$NB209 colors and the dotted black lines are their 1σ errors.

1. We first generate 561 LAEs with a given EW value, and assign to each one of the 561 positions on the FoV of the real objects without duplication. Then, assuming that the (Lyα) redshift distribution of our LAEs is same as the shape of the NB387 response function, with a peak at $z = 2.18$ and an FWHM of $\Delta z = 0.075$, we randomly select a redshift for each of the 561 objects from this distribution.

2. Spectroscopic observations of high-redshift star-forming galaxies have found that the redshift measured from Lyα line is offset from the nebular-line redshift by a few hundred $\mathrm{km\,s^{-1}}$, due to radial acceleration of the circumgalactic gas emitting the line (e.g., Pettini et al. 2001; Steidel et al. 2010; McLinden et al. 2011; Finkelstein et al. 2011). We randomly assign a redshift offset to each of the 561 objects simulated in step 1, assuming that the offsets obey the distribution function obtained by Steidel et al. (2010) for $z \sim 2$ galaxies[19]. Each object is thus given an [O II] redshift.

3. For each object we calculate f_λ^J and $f_\lambda^{\mathrm{NB118}}$ using the EW, continuum spectrum, [O II] redshift, and the NB118 response function at the position of the object on the FoV. We then sum the 561 objects' f_λ^J and $f_\lambda^{\mathrm{NB118}}$, and divide the former by the latter to obtain the $J-$NB118 color of the stacked object.

4. We repeat steps $1-3$ 500 times to obtain the probability distribution of $J-$NB118 color for the given EW.

Figure 8 shows the results of the simulations, i.e., the distribution of $J-$NB118 and $K-$NB209 color as a function of EW. In each panel, the color contour indicates the probability of $J-$NB118 or $K-$NB209 at given EWs, and the solid line and two dotted lines indicate the central value and the 1σ lower and upper limits, respectively, of the observed color. We translate the observed colors and their errors into EWs in the following manner. First, we assume that for each of $J-$NB118 and $K-$NB209, the probability distribution of the true value is a Gaussian with its σ equal to the observed 1σ error in that color. Next, we randomly select a color following this Gaussian probability distribution, and assign to it an EW based on the EW probability distribution against color shown in Figure 8. We repeat this procedure 10,000 times. Finally, we sort the 10,000 EWs in ascending order, and regard the 50 %-tile, 16%-tile, and 84 %-tile as the central value, 1σ lower limit, and 1σ upper limit, respectively. From the translation procedures, we obtain $\mathrm{EW_{rest}}$ for [O II] and Hα+[N II]:

$$\begin{aligned}
\mathrm{EW_{rest,NB118sub}}([\mathrm{OII}]) &= 106^{+14}_{-12}\,\text{Å}\\
\mathrm{EW_{rest,NB209sub}}([\mathrm{OII}]) &= 96^{+23}_{-19}\,\text{Å}. \qquad (5)\\
\mathrm{EW_{rest,NB209sub}}(\mathrm{H}\alpha+[\mathrm{NII}]) &= 271^{+242}_{-104}\,\text{Å}
\end{aligned}$$

The errors in EW correspond to 1σ. The large scatter in $\mathrm{EW_{rest,NB209sub}}$(Hα+[N II]) is due to the large photometric error of $K-$NB209 (see Equation (3)) and the large variance of the NB209 passband over the FoV.

We calculate the [O II] and Hα fluxes from the EWs obtained here combined with the total magnitudes derived in §4.1.1, and convert them into luminosities. These values are summarized in Table 4.

We estimate the Lyα EW in a similar manner to what we explain above; we run the same Monte Carlo simulation skipping step 2, and then translate the u^*-NB387 color into the Lyα EW. The Lyα $\mathrm{EW_{rest}}$ derived for the NB118 (NB209) sub-region is 86^{+3}_{-2} (63^{+3}_{-5}) Å, from which we obtain the observed Lyα luminosity to be $2.11^{+0.04}_{-0.03}\times10^{42}$ ($1.80^{+0.05}_{-0.07}\times10^{42}$) $\mathrm{erg\,s^{-1}}$ (Table 4).

From previous narrow-band surveys, LAEs with $L(\mathrm{Ly}\alpha) = 10^{42} - 10^{44}$ $\mathrm{erg\,s^{-1}}$ are referred to as typi-

---

[19] Although LAEs are so far found to have systematically smaller velocity offsets than LBGs, $\sim 150\,\mathrm{km\,s^{-1}}$ for LAEs (McLinden et al. 2011; Finkelstein et al. 2011) while $\sim 400\,\mathrm{km\,s^{-1}}$ for LBGs (Steidel et al. 2010), we use the data of Steidel et al. (2010) since it is based on much a larger number of measurements (> 40 LBGs while 4 LAEs) and thus statistically more reliable. In any case, the wavelength shift caused by velocity offset is much smaller than that due to the variation of the response curve over the FoV (∼ 15Å by a velocity offset of $\sim 400\,\mathrm{km\,s^{-1}}$ while up to ∼ 150Å by the positional variation for NB118).

TABLE 5
PROPERTIES OF INDIVIDUAL OBJECTS

ID	R.A.$^{(1)}$	Dec.$^{(1)}$	$\mathrm{EW}_{\mathrm{Ly}\alpha}$ (2)	$L_{\mathrm{Ly}\alpha}$ (3)	$\mathrm{EW}_{[\mathrm{OII}]}$ (4)	$L_{[\mathrm{OII}]}$ (5)	$\mathrm{EW}_{\mathrm{H}\alpha+[\mathrm{NII}]}$ (6)	$L_{\mathrm{H}\alpha+[\mathrm{NII}]}$ (7)
NB387-C-06908	02:17:57.113	-05:06:37.06	45^{+9}_{-7}	$4.58^{+0.71}_{-0.65}$	277^{+154}_{-93}	$3.90^{+0.17}_{-0.22}$	...	...
NB387-C-22326	02:17:11.390	-04:51:14.10	54^{+23}_{-17}	$1.56^{+0.49}_{-0.42}$	...	...	198^{+67}_{-55}	$2.93^{+0.28}_{-0.34}$
NB387-C-26967	02:17:19.875	-04:46:54.76	31^{+13}_{-10}	$0.96^{+0.33}_{-0.28}$	22^{+10}_{-8}	$2.27^{+0.56}_{-0.65}$	...	...
NB387-N-01923	02:17:55.840	-04:47:40.11	121^{+32}_{-24}	$4.87^{+0.75}_{-0.68}$	127^{+32}_{-26}	$3.81^{+0.18}_{-0.21}$	...	...
NB387-S-25047	02:17:32.417	-05:12:51.09	31^{+3}_{-2}	$19.43^{+1.39}_{-1.35}$	18^{+2}_{-2}	$6.90^{+0.48}_{-0.50}$	...	...
NB387-W-00165	02:17:07.486	-04:53:53.75	59^{+16}_{-13}	$3.45^{+0.72}_{-0.64}$	35^{+19}_{-15}	$1.40^{+0.32}_{-0.39}$	...	...
NB387-W-00372	02:17:04.957	-04:45:35.62	32^{+7}_{-6}	$4.94^{+0.95}_{-0.87}$	20^{+9}_{-7}	$1.63^{+0.40}_{-0.45}$	...	...
NB387-W-02225	02:16:46.049	-04:59:05.44	39^{+12}_{-10}	$1.82^{+0.44}_{-0.40}$	10^{+8}_{-7}	$0.86^{+0.45}_{-0.53}$	...	...
NB387-W-04041	02:16:28.164	-04:45:17.72	63^{+18}_{-14}	$2.99^{+0.62}_{-0.55}$	75^{+19}_{-16}	$3.87^{+0.27}_{-0.31}$	406^{+66}_{-58}	$6.80^{+0.20}_{-0.22}$
NB387-W-04492	02:16:23.751	-04:57:57.92	43^{+13}_{-11}	$2.31^{+0.55}_{-0.49}$	92^{+37}_{-28}	$2.98^{+0.26}_{-0.32}$	68^{+27}_{-24}	$2.08^{+0.43}_{-0.51}$
NB387-W-06136	02:16:07.936	-05:00:07.96	40^{+8}_{-7}	$5.50^{+0.94}_{-0.87}$	12^{+3}_{-3}	$2.44^{+0.47}_{-0.50}$	...	...

(1) Coordinates are in J2000.
(2) Rest-frame equivalent width of Lyα in unit of Å.
(3) Lyα luminosity in unit of $10^{42}\,\mathrm{erg\,s^{-1}}$.
(4) Rest-frame equivalent width of [O II] in unit of Å.
(5) [O II] luminosity in unit of $10^{42}\,\mathrm{erg\,s^{-1}}$.
(6) Rest-frame equivalent width of Hα+[N II] in unit of Å.
(7) Hα+[N II] luminosity in unit of $10^{42}\,\mathrm{erg\,s^{-1}}$.

cal LAEs (e.g., Gronwall et al. 2007; Ouchi et al. 2008) Therefore, the stacked LAEs we obtain are expected to have average properties of LAEs with $L(\mathrm{Ly}\alpha) > 10^{42}$.

4.2. *Individual Objects*

Seventeen out of the 561 LAE candidates in the NB118 sub-region are detected in NB118 at $\geq 5\sigma$ levels, among which ten have $J-$NB118 ≥ 0.0 and NB118 $<$ NB118$\,(5\sigma)$[20], indicative of the presence of [O II] emission. A detailed calculation using the continuum spectrum from the SED fitting shows that these detection criteria correspond to $\mathrm{EW_{rest}}([\mathrm{O\,II}]) \gtrsim 7\,$Å and $f([\mathrm{O\,II}]) \gtrsim 1.2 \times 10^{-17}\ \mathrm{erg\,s^{-1}\,cm^{-2}}$. Similarly, seven out of the 105 objects in the NB209 sub-region are detected in NB209 at $\geq 5\sigma$ levels, among which three has $K-$NB209 > 0.3 and NB209 $<$ NB209$\,(5\sigma)$, indicative of the presence of Hα+[N II] emission at more than the 5σ level. These detection criteria correspond to $\mathrm{EW_{rest}}(\mathrm{H}\alpha+[\mathrm{N\,II}]) \gtrsim 22\,$Å and $f(\mathrm{H}\alpha+[\mathrm{N\,II}]) \gtrsim 2.1 \times 10^{-17}\ \mathrm{erg\,s^{-1}\,cm^{-2}}$. Two of the H$\alpha$+[N II] detected objects (NB387-W-04041 and NB387-W-04492) are also detected in [O II], while one (NB387-C-22326) is not detected in [O II], probably due to a variation of dust extinction and the complicated origin of the [O II] luminosity (see §6.1.2). The EWs and line luminosities of these objects are summarized in Table 5.

4.3. *Average EWs and Luminosities of [O II] and Hα*

Before presenting the physical properties derived from [O II] and Hα emission lines, we summarize the strengths of these lines of the stacked LAEs.

The stacked object from the NB118 sub-region has $\mathrm{EW}([\mathrm{O\,II}]) = 106^{+14}_{-12}\,$Å and $L([\mathrm{O\,II}]) = 3.54^{+0.11}_{-0.11} \times 10^{41}\,\mathrm{erg\,s^{-1}}$. This EW([O II]) is much larger than those obtained for typical high-z galaxies (e.g., $z \sim 1$ galaxies from the DEEP2 survey; Cooper et al. 2006).

The stacked object from the NB209 sub-region has $\mathrm{EW}(\mathrm{H}\alpha+[\mathrm{N\,II}]) = 271^{+242}_{-104}\,$Å and $L(\mathrm{H}\alpha+[\mathrm{N\,II}]) = 7.98^{+1.17}_{-1.15} \times 10^{41}\,\mathrm{erg\,s^{-1}}$, which correspond to EW(Hα) $= 256^{+229}_{-98}\,$Å and $L(\mathrm{H}\alpha) = 7.55^{+1.11}_{-1.10}\,\mathrm{erg\,s^{-1}}$ after subtraction of [N II] emission (see §6.1.1). This EW(Hα) is larger than those obtained for other high-z galaxies; e.g., Erb et al. (2006b) performed Hα spectroscopy of $z \sim 2$ UV-selected galaxies to find the median EW(Hα) $\sim$ 170Å (Note that EW(Hα) of UV-selected galaxies from Hα spectroscopy may be biased high, since objects with stronger Hα emission can be observed more easily). Recently, Cowie et al. (2011) have found that the bulk ($\sim 75\,\%$) of the local LAEs have EW(Hα) $> 100\,$Å. Thus, it seems that a large Hα EW is a common character of LAEs irrespective of redshift.

5. SED FITTING

We perform SED fitting for the stacked objects in the NB118 sub-region and the NB209 sub-region to infer their stellar populations. We note that the stacked objects used for the SED fitting are not exactly the same as those presented in §4.1, but the stacking is performed only for objects with *Spitzer*/IRAC 3.6, 4.5, 5.8, and 8.0μm photometry from the *Spitzer* legacy survey of the UDS field (SpUDS; *Spitzer* Proposal ID 40021; PI: J. Dunlop) so that stellar population parameters be well constrained[21]. After removing objects with any confusion from neighboring objects in the IRAC images by eye, we stack 304 and 55 LAE candidates in the NB118 sub-region and the NB209 sub-region, respectively.

The procedure of the SED fitting is the same as that of Ono et al. (2010b), except for a fixed redshift (z = 2.18). We use the stellar population synthesis model GALAXEV (Bruzual & Charlot 2003) for stellar SEDs, and include nebular emission (Schaerer & de Barros 2009). A Salpeter initial mass function (IMF; Salpeter

---

[20] The 5σ limiting magnitude here is defined with aperture sizes of 3.″2 diameter for NB118 and 2.″5 diameter for NB209, and estimated to be $\simeq 22.9$ and $\simeq 22.4$, respectively.

[21] We demand only IRAC coverage, not IRAC detection.

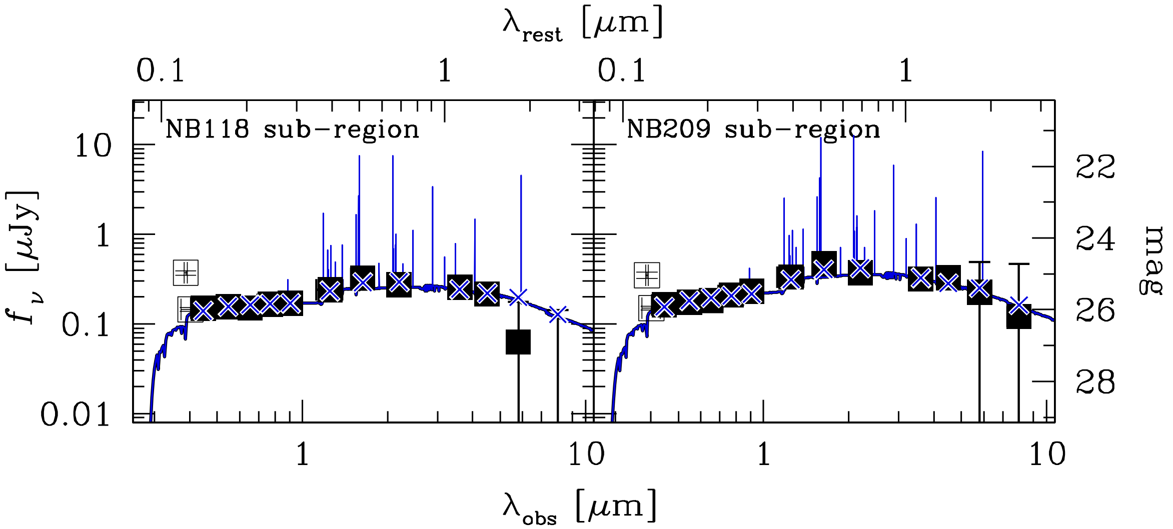

FIG. 9.— Results of SED fitting for the stacked objects in the NB118 sub-region (left) and the NB209 sub-region (right). The filled squares show the observed flux densities used for the fitting (B, V, R, i', z', J, H, K, [3.6], [4.5], [5.8], and [8.0]), while the open squares indicate those not used for the fitting (u^* and NB387). The blue lines show the best-fit model spectra, and the blue crosses correspond to the best-fit flux densities.

TABLE 6
BROADBAND PHOTOMETRY OF THE STACKED LAEs FOR SED FITTING

sample	B	V	R	i'	z'	J	H	K	[3.6]	[4.5]	[5.8]	[8.0]
NB118 sub-region	25.96 (29.31)	25.93 (29.28)	25.95 (29.29)	25.85 (29.20)	25.82 (29.13)	25.44 (28.60)	25.12 (28.06)	25.30 (28.41)	25.38 (28.56)	25.56 (28.08)	26.90 (26.26)	99.99 (26.00)
NB209 sub-region	25.87 (29.20)	25.80 (29.11)	25.75 (29.07)	25.60 (28.93)	25.48 (28.73)	25.09 (28.06)	24.72 (27.38)	24.96 (27.86)	25.13 (27.62)	25.11 (27.28)	25.51 (25.35)	26.19 (25.04)

NOTE. — Broadband photometry of the stacked objects whose stackings are performed for objects with IRAC coverage (see §5). All magnitudes are total magnitudes. 99.99 mag means negative flux densities. Magnitudes in parentheses are 1σ uncertainties adopted in SED fitting.

TABLE 7
PHYSICAL PROPERTIES OF THE STACKED OBJECTS FROM SED FITTING

sample	$f_{\rm esc}^{\rm ion}$	Z [$Z_\odot$]	$M_\star$ [$10^8 M_\odot$]	$E(B-V)_\star$ [mag]	Age [Myr]	χ_r^2
NB118 sub-region	$0.7^{+0.1}_{-0.3}$	0.2	$2.88^{+0.43}_{-0.13}$	$0.21^{+0.02}_{-0.04}$	$12.6^{+17.6}_{-2.6}$	1.678
NB209 sub-region	$0.8^{+0.0}_{-0.1}$	0.2	$4.79^{+0.22}_{-0.81}$	$0.27^{+0.01}_{-0.03}$	$8.32^{+1.68}_{-1.40}$	1.661

NOTE. — Derived physical properties and their 1σ errors of the stacked objects from SED fitting. Z is fixed to $0.2Z_\odot$. The degree of freedom is 8. The results may suffer from additional errors due to degeneracy with age or stellar metallicity, and due to possible systematic uncertainties.

1955) is assumed. We choose constant star formation history and the stellar metallicity $Z = 0.2\,Z_\odot$ since previous studies have shown that most LAEs are young, and that constant star formation history and subsolar stellar metallicities are reasonable assumptions. Since we include nebular emission in the fitting, varying star formation history and stellar metallicity makes the fitting too complicated. Guaita et al. (2011) performed SED fitting to $z \sim 2.1$ stacked LAEs with three scenarios of star formation histories, exponentially increasing, decreasing, and constant star formation, to find equally good fits to the data. They also note that among the free parameters SED fitting can relatively well constrain stellar mass and dust extinction, which are of particular interest in this paper. We also note that the assumption of subsolar metallicity is consistent with the gas-phase metallicity derived for our stacked LAE (see §6.2). For dust extinction, we use Calzetti's extinction law (Calzetti et al. 2000) on the assumption of $E(B-V)_{\rm gas} = E(B-V)_\star$ as proposed by Erb et al. (2006b). IGM attenuation is calculated using the prescription given by Madau (1995). We do not use u^* and NB387 data since they are significantly contaminated by strong Lyα emission. Table 6 summarizes the broadband photometry of the stacked objects that are used for SED fitting. The uncertainties in optical and NIR band photometry listed in Table 6 contain photometric and two systematic errors. The photometric errors are estimated in the same manner as explained in §4.1.1, and the two systematic errors, associated with aperture correction and zero point, are given as follows; the errors in aperture correction are estimated to be $0.01-0.03$ mag using point sources, while the zero-point uncertainties are assumed to be 0.05 mag for every optical and NIR band (inferred by Furusawa et al. (2008) for optical bands). The photometric and two systematic errors are added in quadrature. For the IRAC channels, we include only photometric errors and do not include any systematic errors since they are unknown and the photometric errors are large enough to be dominant uncertainties. Inclusion of systematic errors to the IRAC channels will not change the results of the SED fitting significantly. More details of the SED fitting will be reported elsewhere (Y. Ono et al. in preparation).

We obtain $M_\star = 2.88^{+0.43}_{-0.13} \times 10^8\,M_\odot$, $E(B-V) = 0.21^{+0.02}_{-0.04}$, and age $= 1.26^{+1.76}_{-0.26} \times 10^7\,\mathrm{yr}$ for the stacked object in the NB118 sub-region, with a reduced chi-squares of $\chi^2_r = 1.68$, and $M_\star = 4.79^{+0.22}_{-0.81} \times 10^8\,M_\odot$, $E(B-V) = 0.27^{+0.01}_{-0.03}$, and age $= 8.32^{+1.68}_{-1.40} \times 10^6\,\mathrm{yr}$ for the stacked object in the NB209 sub-region, with $\chi^2_r = 1.66$. Table 7 summarizes the physical properties derived from the SED fitting, and Figure 9 shows the best-fit model spectra with the observed flux densities. The errors in the best-fit parameters correspond to the 1σ confidence interval ($\Delta\chi^2 < 1$) for each parameters. The relatively small errors of the results are due to the small uncertainties adopted in the SED fitting. We note that the results from the SED fitting may suffer from additional errors due to degeneracy with age or stellar metallicity, and due to other possible systematic uncertainties such as the position matching, and in the assumption of star formation history and stellar metallicity. The discussion will be expanded more in Y. Ono et al. (in preparation).

Although the dust extinction of our LAEs is rather high compared with those of higher-z LAEs ($E(B-V) = 0.00 - 0.07$ at $z \sim 3$; e.g., Nilsson et al. 2007; Ono et al. 2010a), such an increasing trend of $E(B-V)$ in LAEs down to $z \sim 2$ is also seen in other studies (Nilsson et al. 2011; Guaita et al. 2011). Nilsson et al. (2011) performed SED fitting to $z \sim 2.3$ LAEs to find that A_V ($E(B-V)$) varies over $0.0 - 2.5$ ($0.00 - 0.61$) with an average of $A_V = 0.6$ ($E(B-V) = 0.15$) and $A_V = 1.5$ ($E(B-V) = 0.37$) for old and young population models, respectively. Guaita et al. (2011) obtained $E(B-V) = 0.22^{+0.06}_{-0.13}$ for stacked $z \sim 2.1$ LAEs assuming constant star formation history. These findings combined with our result may indicate a strong evolution of dust extinction in LAEs from $z > 3$ to $z \sim 2$.

6. RESULTS AND DISCUSSION

6.1. *Star Formation Rate*

6.1.1. *Deriving SFR from the Hα Luminosity*

The Hα luminosity is believed to be the most reliable SFR indicator of galaxies among those based on the rest-frame UV and optical spectral features. Indeed it is proportional to the birth rate of massive stars as well as being relatively insensitive to dust extinction as compared with UV-continuum. We measure the SFR of the stacked object in the NB209 sub-region from its Hα luminosity using the relation (Kennicutt 1998):

$$\mathrm{SFR}[M_\odot\ \mathrm{yr}^{-1}] = 7.9 \times 10^{-42} L(\mathrm{H}\alpha)\ \mathrm{erg\ s}^{-1}. \quad (6)$$

Before applying this relation, however, we have to subtract the contribution from [N II]$\lambda\lambda 6584, 6548$ lines from the observed Hα+[N II] luminosity. It is known that the [N II]/Hα ratio varies with metallicity; indeed, this ratio is used as a metallicity indicator of galaxies, called the $N2$ index (e.g., Pettini & Pagel 2004; Maiolino et al. 2008). In Table 4, we derive $L(\mathrm{H}\alpha+[\mathrm{N\,II}])$ to be $8.0^{+1.3}_{-1.2} \times 10^{41}\,\mathrm{erg\,s^{-1}}$. We use the metallicity estimated in §6.2 to infer $L([\mathrm{N\,II}])/L(\mathrm{H}\alpha) = 5.7^{+1.7}_{-1.3} \times 10^{-2}$ (Maiolino et al. 2008). The Hα luminosity is then $8.0^{+1.3}_{-1.2} \times 10^{41}/(1+5.7^{+1.7}_{-1.3} \times 10^{-2}) = 7.6^{+1.2}_{-1.2} \times 10^{41}\,\mathrm{erg\,s^{-1}}$, from which we obtain SFR $= 6^{+1}_{-1}\,M_\odot\,\mathrm{yr}^{-1}$.

With $E(B-V) = 0.27^{+0.01}_{-0.03}$ combined with Calzetti et al. (2000)'s extinction law, we obtain the dust-corrected Hα luminosity to be $1.7^{+0.3}_{-0.3} \times 10^{42}\,\mathrm{erg\,s^{-1}}$, which is translated into SFR $= 14^{+2}_{-3}\,M_\odot\,\mathrm{yr}^{-1}$. This SFR is the first unbiased SFR estimate from Hα luminosity for typical $z \sim 2$ LAEs of $L(\mathrm{Ly}\alpha) > 1 \times 10^{42}\ \mathrm{erg\,s^{-1}}$. Although Finkelstein et al. (2011) have derived SFRs for two $z \sim 2.3 - 2.5$ LAEs from Hα spectroscopy, both objects have $L(\mathrm{Ly}\alpha) \sim 2 \times 10^{43}\ \mathrm{erg\,s^{-1}}$, which is about one order of magnitude brighter than typical Lyα luminosities of LAEs from narrow-band surveys (e.g., Ouchi et al. 2008), due to pre-selection of bright objects for NIR spectroscopy. Hayes et al. (2010) have measured $L(\mathrm{H}\alpha)$ for six LAEs with $L(\mathrm{Ly}\alpha) = (0.3 - 4.5) \times 10^{42}\ \mathrm{erg\,s^{-1}}$ for which Hα emission is detected. In contrast to these studies, our study is based on a large number ($N = 105$) of purely Lyα-selected galaxies.

SED fitting of the stacked object in the NB209 sub-region gives a stellar mass of $5 \times 10^8\,M_\odot$. Therefore, the stacked object has the SFR and the stellar mass of the same order of magnitudes of those of LAEs studied earlier from SED fitting ($z \sim 2$: Guaita et al. 2011, $z \sim 3$: Gawiser et al. 2006, 2007; Lai et al. 2008; Nilsson et al. 2007; Ono et al. 2010a). Some studies have derived SFRs of LAEs from (dust-uncorrected) UV-continuum (e.g., Gronwall et al. 2007; Ouchi et al. 2008, 2010; Nilsson et al. 2009, 2011; Guaita et al. 2010) which are roughly in the range $1 - 10\,M_\odot\,\mathrm{yr}^{-1}$, comparable to our dust-uncorrected SFR.

We also estimate in a similar manner the SFRs of the (Hα+[N II])-detected objects, NB387-C-22326, NB387-W-04041, and NB387-W-04492 to be 23^{+2}_{-3}, 51^{+2}_{-2}, and 13^{+3}_{-3} $M_\odot\,\mathrm{yr}^{-1}$, respectively[22]. These SFRs are much larger than that of a typical LAE at $z \sim 2$, but similar to some bright LAEs at similar redshifts (Nilsson et al. 2011; Finkelstein et al. 2011). This is because our NIR narrowband images are relatively shallow, and only bright, massive LAEs with high SFR are likely to be detected. Indeed, Nilsson et al.'s and Finkelstein et al.'s LAEs are much more massive than a typical LAE ($\gtrsim 10^{10}\,M_\odot$) with some exceptions like HPS256 (Finkelstein et al. 2011) whose mass can be as small as $6 \times 10^8\,M_\odot$. Although the (Hα+[N II])-detected objects lack Spitzer/IRAC data and their stellar masses are poorly constrained by SED fitting, rough estimate

---

[22] For NB387-C-22326, we assume $L(\mathrm{H}\alpha+[\mathrm{N\,II}]) = L(\mathrm{H}\alpha)$, since its [O II] is not detected and therefore its metallicity is low enough that the contribution of [N II] to $L(\mathrm{H}\alpha+[\mathrm{N\,II}])$ is considered to be negligible. For NB387-W-04492, we adopt solar metallicity from the empirical [O II]/(Hα+[N II])-metallicity relation (see §6.2.1) to correct for [N II] emission. For NB387-W-04041, the metallicity is estimated to be $12 + \log(\mathrm{O/H}) \sim 8.1$ with Equation (8). All SFRs are calculated assuming dust free.

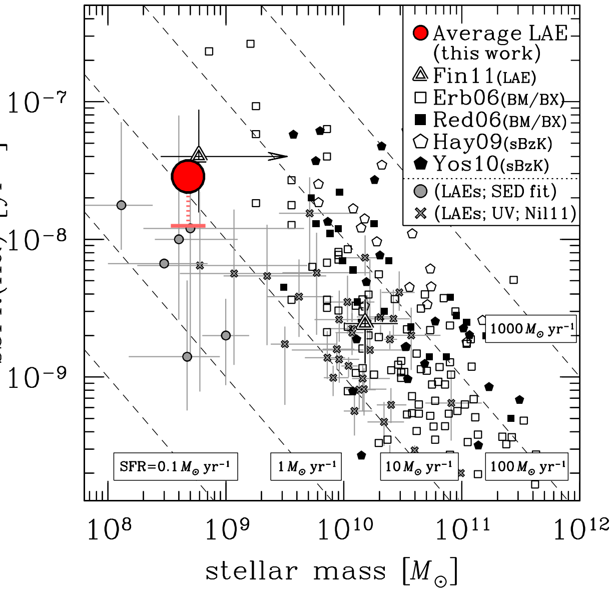

Fig. 10.— Specific SFR (sSFR) vs. stellar mass for various types of galaxies at $z \sim 2$. The red large filled circle indicates our result after correction for dust extinction of $E(B-V) = 0.27$, while the red horizontal bar indicates the sSFR on the assumption of $E(B-V) = 0$. The triangles are LAEs with Hα measurements (Finkelstein et al. 2011). The squares are UV-selected galaxies (open: Erb et al. 2006b, filled: Reddy et al. 2006) and the pentagons are sBzK galaxies (open: Hayashi et al. 2009, filled: Yoshikawa et al. 2010). All sSFRs are derived from Hα luminosities after dust correction. A Salpeter IMF is assumed for all objects. The dashed lines correspond to constant SFRs of $0.1, 1, 10, 100, 1000\,M_\odot\,\mathrm{yr}^{-1}$. The gray filled circles with errorbars are $z = 2-3$ stacked LAEs whose SFRs are estimated from SED fitting (Guaita et al. 2011; Nilsson et al. 2007; Gawiser et al. 2006, 2007; Lai et al. 2008; Ono et al. 2010a), and the gray crosses are $z = 2.3$ LAEs whose SFRs are estimated from UV-continuum (Nilsson et al. 2011).

is possible from their K-band magnitudes. Daddi et al. (2004), for instance, derived a relation between K magnitude and mass for $z \sim 2$ BzK galaxies. The K-band total magnitudes of NB387-C-22326, NB387-W-04041, and NB387-W-04492 are 23.28, 23.02, and 22.39, which correspond to a stellar mass of $(2-3)\times10^{10}$, $(2-4)\times10^{10}$, and $(4-7)\times10^{10}\,M_\odot$, respectively, following Daddi et al.'s simple relation. Although this is just a rough estimate and the relation itself involves a certain uncertainty ($\sigma(\Delta\log M_*) \sim 0.2$; Daddi et al. 2004), the individually (Hα+[N II])-detected objects are likely to be massive LAEs.

6.1.2. *Deriving SFR from the [O II] Luminosity*

The [O II] luminosity is also known to be a useful SFR indicator (e.g., Gallagher et al. 1989; Kennicutt 1992, 1998; Kewley et al. 2004; Moustakas et al. 2006) and frequently used to derive SFRs of galaxies at high-z, where Hα cannot be accessed from the ground (e.g., Teplitz et al. 2003; Hopkins 2004; Takahashi et al. 2007). The SFR is derived from the [O II] luminosity using the relation (Kennicutt 1998):

$$\mathrm{SFR}[M_\odot\ \mathrm{yr}^{-1}] = (1.4\pm0.4)\times10^{-41}L([\mathrm{OII}])\ \mathrm{erg\ s}^{-1} \quad (7)$$

In Table 4, we derive L([O II]) in the NB209 sub-region to be $5.3^{+0.4}_{-0.4}\times10^{41}$ erg s^{-1}, which corresponds to SFR $= 7^{+2}_{-2}\,M_\odot\,\mathrm{yr}^{-1}$. This is consistent with the SFR derived from the Hα luminosity when dust free is assumed. However, if we take into account the dust extinction of $E(B-V) = 0.27^{+0.01}_{-0.03}$, we find that the SFR derived from the [O II] luminosity could be more than twice the SFR derived from the Hα luminosity, and they are not consistent within 1σ errors: $\mathrm{SFR_{cor}}(\mathrm{H}\alpha) = 14^{+2}_{-3}\,M_\odot\,\mathrm{yr}^{-1}$, and $\mathrm{SFR_{cor}}([\mathrm{O\,II}]) = 32^{+9}_{-11}\,M_\odot\,\mathrm{yr}^{-1}$. Such differences have also been reported for present-day galaxies (e.g., Gilbank et al. 2010) and for high-z galaxies (e.g., Charlot et al. 2002; Tresse et al. 2002). The difference can be due to the complicated origin of the [O II] luminosity. The [O II] luminosity is not directory proportional to the ionizing luminosity, and also depends on the chemical abundance and excitation state of the ionized gas (e.g., Kennicutt 1998; Kewley et al. 2004; Moustakas et al. 2006). Indeed, the ratio of [O II]/Hβ can be used as a metallicity indicator (e.g., Nagao et al. 2006; see also §6.2.1). Alternatively, the uncertainty of the dust correction may cause the difference of the SFRs. The relatively large dust correction for the [O II] luminosity makes it difficult to derive the SFR accurately (e.g., Jansen et al. 2001). The difference of the SFRs of our result may be also due to the overestimates of the dust extinction inferred from the SED fitting. In any case, we use the SFR derived from the Hα luminosity, which is more directory proportional to the SFR and less affected by the dust attenuation or other factors (e.g., metallicity), in the following analysis.

6.1.3. *Mass-sSFR Relation*

We plot the stacked object on the specific SFR (sSFR $\equiv \mathrm{SFR}/M_\star$) vs. stellar mass plane in Figure 10. Although sBzK and UV-selected galaxies obey a simple scaling relation between the sSFR and the stellar mass, our stacked LAE is located below an extrapolation of this relation toward lower-mass, even though the dust extinction of $E(B-V) = 0.27$ is taken into account in the SFR. We note that the other LAEs whose SFR and stellar mass are derived by SED fitting (gray symbols) are also distributed below the extrapolation. If LAEs are typical of low-mass galaxies, this figure indicates that low-mass galaxies with $M \lesssim 10^{9-10}\,M_\odot$ have lower star formation efficiencies than extrapolated from more massive galaxies. This trend, if real, is qualitatively consistent with galaxy formation models which predict that less massive systems have low star formation efficiencies owing to various mechanisms such as feedback from supernovae (see, e.g., Benson 2010 for a review).

6.2. *Metallicity*

6.2.1. *Constraining the Metallicity*

An accurate estimate of gas phase metallicity requires knowledge of the electron temperature which is provided by comparing auroral lines to nebular emission lines (e.g., [O III]$\lambda4363/\lambda5007$; *direct T_e method*; Lee et al. 2004). However, auroral lines are generally weak and it is difficult to observe them in distant galaxies. A number of empirical relations between the ratio of nebular lines and metallicity have been proposed to measure gas-phase metallicities of distant galaxies. Among them, we combine the [N II]$\lambda6584$/Hα indicator ($N2$ index: e.g., Pettini & Pagel 2004; Maiolino et al.

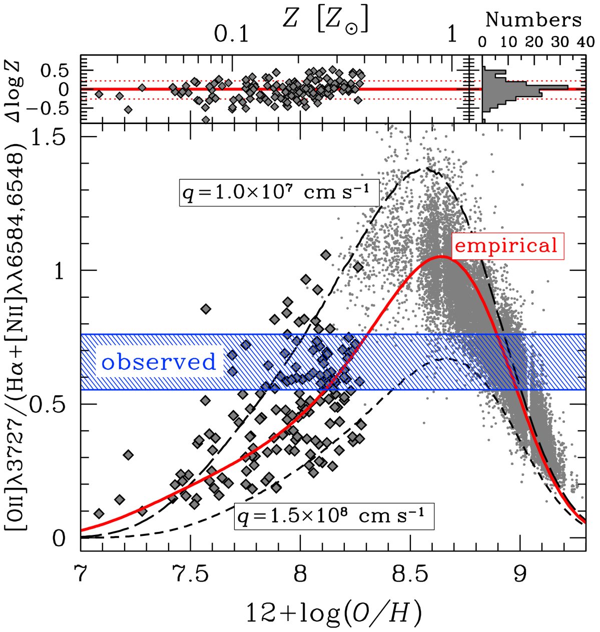

Fig. 11.— (bottom) Relation between [O II]λ3727/(Hα+[N II]$\lambda\lambda$6584, 6548) and gas-phase metallicity. The red solid line corresponds to the empirical relation given by Equation (8) combined with Equation (9). The gray diamonds represent low-metallicity galaxies compiled by Nagao et al. (2006) whose metallicities are inferred through the *direct* T_e *method* and then used in Maiolino et al. (2008) to fit the polynomials in Equation (9) in the range $12 + \log Z < 8.3$; they are distributed around the best-fit line with a large scatter ($\Delta \log Z \sim 0.2$). The gray dots are SDSS galaxies (Kewley & Dopita 2002) used for the fit in the range of $12 + \log Z > 8.3$ whose metallicities are inferred through photoionization models. The dashed and long-dashed lines correspond to the relations derived from a combination of stellar population synthesis and photoionization models with an ionization parameter of $q = 1.5 \times 10^8$ and $1.0 \times 10^7\,\mathrm{cm\,s^{-1}}$, respectively (Kewley & Dopita 2002). We ignore the range $Z > Z_\odot$ in this paper, because LAEs are found to be metal-poor in previous studies (see §6.2.1). The blue shaded area is the range of [O II]λ3727/(Hα+[N II]$\lambda\lambda$6584, 6548) for the stacked object assuming $E(B-V) = 0$. (top) Residuals from the best-fit polynomials for the low-metallicity galaxies (left) and their histogram (right). The two dotted lines show the rms of the residuals for $\Delta \log Z > 0$ objects (rms= 0.22) and $\Delta \log Z < 0$ objects (0.26), respectively.

2008) and the [O II]/Hβ indicator (e.g., Nagao et al. 2006; Maiolino et al. 2008) to derive the metallicity of our object. Even for the same metallicity index, however, calibrations are often different among the authors, leading to different metallicity measures as discussed in Nagao et al. (2006). As for the $N2$ index, Nagao et al. (2006)'s calibration and Pettini & Pagel (2004)'s agree well ($\Delta Z < 0.2\,$dex) with each other over $7.7 < 12 + \log(\mathrm{O/H}) < 8.5$, while out of this range a large difference is seen probably due to the lack of objects for calibration in Pettini & Pagel (2004) sample. We use the calibration by Maiolino et al. (2008), which is an update of Nagao et al. (2006), based on a low-Z sample ($7.7 < 12 + \log(\mathrm{O/H}) < 8.3$).

We cannot, however, apply these indicators directly to our object, because we have only [O II] and Hα+[N II] fluxes. Instead, we make use of the fact that [O II]/(Hα+[N II]) ratio can be expressed as a combination of the two indicators:

$$\frac{[\mathrm{OII}]}{(\mathrm{H}\alpha + [\mathrm{NII}]\lambda\lambda6584, 6548)} = \frac{1}{2.85}\frac{[\mathrm{OII}]/\mathrm{H}\beta}{(1 + 1.33 \times [\mathrm{NII}]\lambda6584/\mathrm{H}\alpha)}, \qquad (8)$$

where we assume that all lines are dust free and adopt an intrinsic Hα/Hβ ratio of 2.85 and an intrinsic [N II]λ6584/λ6548 ratio of 3.0 (Osterbrock 1989). The effect of dust extinction will be discussed later. The metallicity dependence of the two indicators is empirically approximated by the polynomial:

$$\log R = c_0 + c_1 x + c_2 x^2 + c_3 x^3 + c_4 x^4, \qquad (9)$$

where $R =$ [O II]/Hβ or [N II]/Hα, x is the metallicity relative to solar (i.e., $x = \log(Z/Z_\odot) = 12 + \log(\mathrm{O/H}) - 8.69$, Allende Prieto et al. 2001), and the coefficients c_0 to c_4 are taken from Table 4 of Maiolino et al. (2008). Thus, [O II]/(Hα+[N II]) ratio is expressed as a function of metallicity, as shown in Figure 11 by the solid curve. In this figure, the gray diamonds and gray dots indicate, respectively, local low-metallicity galaxies with $12 + \log(\mathrm{O/H}) < 8.3$ (Nagao et al. 2006) and SDSS galaxies with $12 + \log(\mathrm{O/H}) > 8.3$ (Tremonti et al. 2004; Kewley & Dopita 2002) used to calibrate Equation (9); the metallicities of the former are measured with the *direct* T_e *method* (Nagao et al. 2006), while those of the latter are derived by applying photoionization models to the most prominent optical emission lines ([O II], Hβ, [O III], Hα, [N II], [S II]). The ratio has a peak at around solar metallicity and for any given value of [O II]/(Hα+[N II]) (except for the peak), there are two solutions of metallicity, one being subsolar and the other being supersolar. The blue shaded region in Figure 11 corresponds to the observed [O II]/(Hα+[N II]$\lambda\lambda$6584, 6548) ratio including the 1σ photometric error: $0.66^{+0.11}_{-0.11}$. Two metallicity ranges are found to meet the observation: $12 + \log(\mathrm{O/H}) = 8.21^{+0.10}_{-0.11}$ and $8.94^{+0.05}_{-0.05}$. The latter range, however, appears to be unlikely, since it is not consistent with recent spectroscopic observations that LAEs have much lower metallicities than the solar value (Finkelstein et al. 2011; Cowie et al. 2011). Modest dust extinction inferred from SED fitting also favors low metallicities (e.g., Gawiser et al. 2006, 2007; Pirzkal et al. 2007; Lai et al. 2008; Ono et al. 2010a). If we rule out the supersolar solution, the metallicity of our object is estimated to be $12 + \log(\mathrm{O/H}) = 8.21^{+0.10}_{-0.11}$, or $Z/Z_\odot = 0.33^{+0.09}_{-0.07}$.

This metallicity estimate, however, involves two systematic uncertainties. First is the uncertainty in the polynomial fit given by Equation (9) for low-metallicity galaxies. The gray diamonds plotted in Figure 11 represent galaxies with $12 + \log(\mathrm{O/H}) < 8.3$ used in Maiolino et al. (2008) to fit the polynomials. The galaxies are distributed around the solid line (as expected), but with a large scatter of $\Delta \log Z = +0.22/-0.26$ (1σ). This may suggest that there are large errors in measurements of line ratios and/or metallicities, since these measurements collected from the literature are based on different methods to measure line ratios (Nagao et al. 2006). Alternatively, such a large scatter may be intrinsic. Dashed lines in Figure 11 represent relations of metallicity and [O II]/(Hα+[N II]) from a combination of stellar population synthesis and photo-ionization models with a set of ionization parameter (q; Kewley & Dopita 2002). From Figure 11, the large scatter could be ex-

TABLE 8
Coefficients for metallicity indicators in Equation (9)

Flux ratio ($\log R$)	c_0	c_1	c_2	c_3	c_4
$\log([\mathrm{N\,II}]\lambda6584/\mathrm{H}\alpha)^{(1)}$	−0.7732	1.2357	−0.2811	−0.7201	−0.3330
$\log([\mathrm{O\,II}]\lambda3727/\mathrm{H}\beta)^{(1)}$	0.5603	0.0450	−1.8017	−1.8434	−0.6549
$\log([\mathrm{O\,II}]\lambda3727/(\mathrm{H}\alpha+[\mathrm{N\,II}]\lambda\lambda6584,6548))^{(2)}$	0.0164	−0.1673	−1.9484	−1.8158	−0.6148

(1) The coefficients are taken from Table 4 of Maiolino et al. (2008).

(2) The coefficients are determined by a best fit polynomial of the combined equation described in Equation (8).

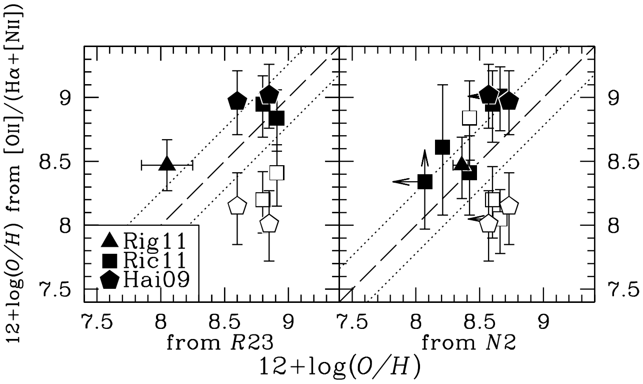

Fig. 12.— Comparison of the metallicity calculated from our $[\mathrm{O\,II}]/(\mathrm{H}\alpha+[\mathrm{N\,II}])$ indicator with those from two frequently used indicators, the $R23$ index (left panel) and the $N2$ index (right panel), for $z \sim 2$ lensed galaxies taken from the literature (Rigby et al. 2011 with triangle; Richard et al. 2011 with squares; Hainline et al. 2009 with pentagons). At each panel, the dashed line is the line of equality, and the dotted lines show the 1σ errors associated with our indicator including the calibration errors ($\Delta \log Z = +0.22/-0.26$; see §6.2.1). Our indicator has in principle two solutions (see §6.2.1), and for galaxies with two solutions over their 1σ errors both metallicities are plotted; solutions with the smaller differences from Z_{R23} or Z_{N2} in black, while those with the larger differences in white.

plained by a diversity of ionization parameters ($q \sim (1-10)\times10^7\,\mathrm{cm\,s^{-1}}$). Note that the empirical line can be reproduced by the Kewley & Dopita's photo-ionization model with $q \sim (4-8)\times10^7\,\mathrm{cm\,s^{-1}}$. In any case, we estimate that the calibration error in our metallicity estimate due to the uncertainty in the polynomial fit is $\Delta\log Z = +0.22/-0.26$ (1σ). In Figure 12, we compare metallicities derived from our original indicator with those from more commonly used indicators: the $R23$ index (($[\mathrm{O\,II}]\lambda3727+[\mathrm{O\,III}]\lambda\lambda4959,5007)/\mathrm{H}\beta$; e.g., Tremonti et al. 2004 and references therein) and the $N2$ index to check robustness of the indicator. We compare the indicators using spectroscopic data of $z \sim 2$ lensed galaxies (Hainline et al. 2009; Richard et al. 2011; Rigby et al. 2011). From the comparison, we see that metallicities from our indicator are roughly consistent with those from other indicators within $\Delta\log Z = +0.22/-0.26$ (1σ).

Second is the uncertainty in dust extinction. While we have assumed $E(B-V)=0$ to derive Equation (8), the SED fit suggests that the stacked object may have $E(B-V)$ up to $\simeq 0.27$ (see §5). We find that adopting $E(B-V)=0.27$ instead of $E(B-V)=0$ increases the metallicity estimate by $\Delta\log Z \simeq 0.3$.

When these two systematic errors are taken into account, the metallicity range of our object is estimated to be $12+\log(\mathrm{O/H}) = 8.21^{+0.10}_{-0.11}\,(\mathrm{random})\,^{+0.22}_{-0.26}\,(\mathrm{calib}) = 8.21^{+0.24}_{-0.28}$, or $Z/Z_\odot = 0.33^{+0.25}_{-0.16}$, assuming $E(B-V)=0$. If $E(B-V)=0.27$ is adopted, the metallicity increases to $12+\log(\mathrm{O/H}) \sim 8.5^{+0.24}_{-0.28}$, or $Z/Z_\odot = 0.7^{+0.5}_{-0.3}$. Recall, however, that our method logically permits the possibility of a supersolar metallicity and that in order to rule out such a possibility, we will require independent data favoring metal-poor LAEs. In this sense, the upper limit of the metallicity obtained above is not as strict as the lower limit. Considering this, we adopt a conservative conclusion that the metallicity of the stacked object is no less than $0.17\,Z_\odot$ (1σ), or $0.09\,Z_\odot$ (2σ). This 2σ lower limit is obtained in the following manner. The observed $[\mathrm{O\,II}]/(\mathrm{H}\alpha+[\mathrm{N\,II}])$ ratio and its 2σ negative photometric error are 0.66 and −0.23, respectively, thus the 2σ lower limit of the observed $[\mathrm{O\,II}]/(\mathrm{H}\alpha+[\mathrm{N\,II}])$ ratio is 0.43, which corresponds to $12+\log(\mathrm{O/H}) = 7.96$. Therefore, the 2σ negative statistical error in terms of metallicity is $(\Delta\log Z)_{\mathrm{calib}} = -(8.21-7.96) = -0.25$. On the other hand, the 2σ negative systematic error is just twice the 1σ value (−0.26), hence $(\Delta\log Z)_{\mathrm{sys}} = -0.52$ (2σ). Therefore, we obtain the 2σ negative error in terms of metallicity as $(\Delta\log Z) = -\sqrt{0.25^2+0.52^2} = -0.58$, and the 2σ lower limit of the metallicity as $12+\log(\mathrm{O/H}) = 8.21-058 = 7.63$, corresponding to $Z = 0.09\,Z_\odot$. We calculate the 3σ, 4σ, and 5σ lower limits of metallicity in the same manner to obtain $12+\log(\mathrm{O/H}) = 7.32$, 6.97, and 6.58, or $Z = 0.04\,Z_\odot$, $0.02\,Z_\odot$, and $0.008\,Z_\odot$, respectively. Although a recent spectroscopic study has placed a weak upper limit on the metallicity of bright LAEs ($Z < 0.56\,Z_\odot$ (2σ)[23]; Finkelstein et al. 2011), this is the first lower limit on the metallicity for typical LAEs at high-z. Scannapieco et al. (2003) proposed that LAEs may be extremely metal poor primordial galaxies, and Schaerer (2003) also found that large Lyα EWs can be observed from extremely metal poor galaxies ($Z/Z_\odot \lesssim 10^{-5}$). However, our firm lower limits, e.g., $Z > 2\times10^{-2}\,Z_\odot$ at the 4σ level, do not support this idea at least for $z=2.2$ LAEs. For higher redshift (> 3) LAEs, on the other hand, their metallicities may be lower than what we derive for $z=2.2$ LAEs, because, as seen in §5, the amount of dust extinction for LAEs decreases with redshift from $z\sim2$ to $z>3$.

6.2.2. *Mass-Metallicity Relation*

Figure 13 shows the observed mass-metallicity ($M-Z$) relation of star-forming galaxies at local and $z \sim 2.2$ compiled by Maiolino et al. (2008): Kewley & Ellison (2008) for $z \sim 0.07$, and Erb et al. (2006a) for $z \sim 2.2$. For $z \sim 2.2$, the relation is derived based on stacked galaxies with $M \gtrsim 3\times10^9\,M_\odot$. The line below the observed

---

[23] We have recalibrated the metallicity given in Finkelstein et al. (2011) using Equation (9). The original metallicity upper limit is $Z < 0.41\,Z_\odot$ (2σ).

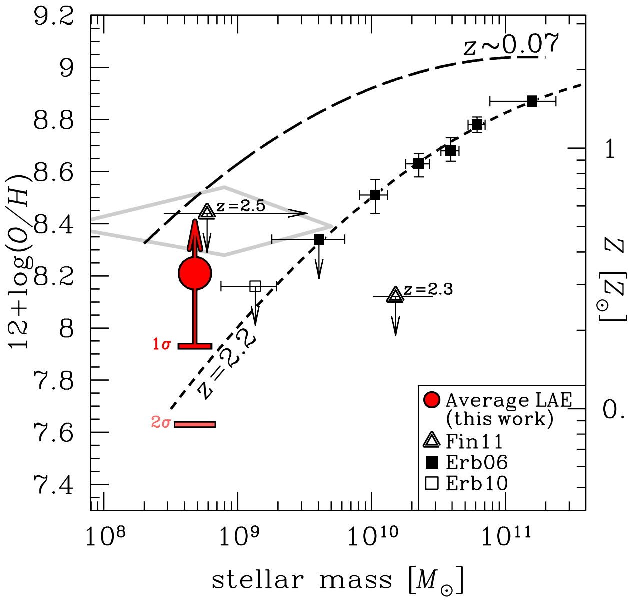

FIG. 13.— Mass-Metallicity ($M - Z$) relation of UV-selected galaxies and LAEs at $z \sim 2$. The red circle with an arrow represents our stacked LAE. The red ticks show the lower limits of metallicity at 1 and 2σ levels as labeled next to the ticks. The open triangles show two LAEs at $z \sim 2.3$ and 2.5 from Finkelstein et al. (2011) whose upper limits denote the 2σ confidence limits. The curves indicate the $M - Z$ relation observed at $z \sim 0.07$ (long-dashed; Kewley & Ellison 2008) and $z \sim 2.2$ (dashed; Erb et al. 2006a) (best-fit functions are determined by Maiolino et al. (2008)). The filled squares are stacked data points of $z \sim 2.2$ UV-selected galaxies in six bins in stellar mass(Erb et al. 2006a), and the open square indicates BX418 ($z = 2.3$; Erb et al. 2010), which is considered to be the most metal-poor UV-selected galaxy. The gray diamond area shows the median stellar mass and metallicity for $z = 0.195 - 0.44$ LAEs and their 1σ ranges (Cowie et al. 2011). All data have been recalibrated to have the same metallicity scale (Maiolino et al. 2008) and IMF (Salpeter 1955) so that all results can be directly compared.

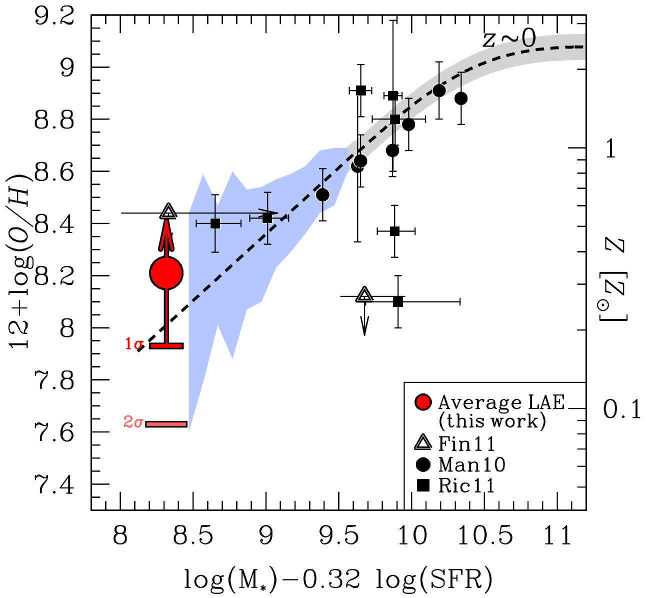

FIG. 14.— Fundamental $M - Z$ relation proposed by Mannucci et al. (2010). The dashed curve indicates the best-fit relation for $z \sim 0$ SDSS galaxies (Mannucci et al. 2010, 2011), whose typical distribution ranges are shown as the gray shaded (for those with $M_\star \gtrsim 10^{9.2}\, M_{\odot,\mathrm{chabrier}}$) and the blue shaded ($M_\star \lesssim 10^{9.2}\, M_{\odot,\mathrm{chabrier}}$) regions. The black circles are $z \sim 2.2$ UV-selected galaxies compiled by Mannucci et al. (2010), the black squares are $1.5 < z < 2.5$ lensed galaxies (Richard et al. 2011), and the open triangles show two LAEs at $z \sim 2.3$ and 2.5 from Finkelstein et al. (2011). The red circle with an arrow is our result; it is located near a smooth extrapolation of the fundamental $M - Z$ relation toward lower stellar masses.

limit of stellar mass is therefore a smooth extrapolation of the best-fit function. The $M - Z$ relation is found to evolve with redshift in the sense that the metallicity at a given stellar mass decreases with increasing redshift up to $z \sim 3.5$ (Maiolino et al. 2008; Mannucci et al. 2009).

The red circle with an upward arrow represents our stacked object in the NB209 sub-region which has a stellar mass of $5 \times 10^8\, M_\odot$ and a metallicity of $Z \gtrsim 0.09\, Z_\odot$ (2σ). The large circle represents the central value, which is derived assuming $E(B - V) = 0$, and the two ticks stand for the 1σ and 2σ lower limits. Note that our study is the first to place a lower limit to the metallicity of $z \sim 2$ galaxies with stellar masses below $10^9 M_\odot$, well below the lower-mass limit of the previous studies. The two triangle symbols correspond to the two LAEs at $z \sim 2.3$ and 2.5 by Finkelstein et al. (2011); for both objects the metallicity estimate is an upper limit. The less massive one of the two has a stellar mass comparable to our object. If Finkelstein et al. observed a typical LAE, then the combination of their results with ours suggests that LAEs with $\lesssim 10^9 M_\odot$ at $z \sim 2$ have metallicities in the range $0.09 \lesssim Z/Z_\odot \lesssim 0.56$ with the 95 % confidence level.

Comparison of our object with the $M - Z$ relation at $z = 2.2$ reveals that our object is consistent with a smooth extrapolation toward lower masses of the $M - Z$ relation at the 1.5σ level. However, we also note that the central value of our object is 0.4 dex larger than the extrapolation. This offset might be real, since our metallicity estimate is a conservative lower limit. If real, there are two possible explanations of this offset. One is that the slope of the $M - Z$ relation may become shallower below the stellar-mass limit of UV-selected galaxies and our object is in fact on the relation, implying that UV-selected galaxies and LAEs obey a common $M - Z$ relation. Although Erb et al. (2010) have recently found an unreddened, low-metallicity, and low-mass UV-selected galaxy (BX418) at $z = 2.3$ (black open square) which seems consistent with the conventional $M - Z$ relation at $z \sim 2$ (Erb et al. 2006a), it is only one object and its upper limit for UV-selected galaxies is still larger than our lower limit. The other possibility is that UV-selected galaxies and LAEs obey different $M - Z$ relations and that the extrapolation is valid only for UV-selected galaxies. In this case, it is likely that LAEs have relatively high metallicities for their masses, unlike the relation estimated for UV-selected galaxies. Although this appears to be inconsistent with the *conventional* picture that LAEs are the most metal-poor population, there are, in fact, few studies which compare metallicities of LAEs and other galaxies statistically at the same stellar mass. Thus, we cannot immediately rule out this possibility.

Recently, Mannucci et al. (2010) have found that the observed dispersion in the $M - Z$ relation is correlated with the SFR in the sense that galaxies with lower SFRs have higher metallicities, and that star-forming galaxies at all redshifts below $z \sim 2.2$ obey a common, single $M - Z-$SFR relation. They referred to the relation as the fundamental $M - Z$ relation. A similar relation between the three quantities is reported by Lala-López et al. (2010), and this trend is also realized for high-z lensed galaxies (Richard et al. 2011), Indeed, the SFR of our object is lower than that of UV-selected galaxies with similar mass, and most interestingly, we find that our object is located near a smooth extrapolation of the fundamental $M - Z$ relation toward lower stellar masses (Figure 14). In Figure 14, the dashed curve shows the fundamental $M - Z$ relation defined by SDSS galaxies (Mannucci et al. 2010, 2011), and the gray and blue shaded areas show the typical distribution ranges of galaxies with $M_\star \gtrsim 10^{9.2}\,M_{\odot,\rm chabrier}$ (Mannucci et al. 2010) and $M_\star \lesssim 10^{9.2}\,M_{\odot,\rm chabrier}$ (Mannucci et al. 2011), respectively. Therefore, the offset seen in the $M - Z$ relation may be due to the relatively low SFR of a typical LAE, and the offset seen in the mass-sSFR relation may be due to the relatively high metallicity for its mass compared to the value estimated from the $M - Z$ relation of UV-selected galaxies.

6.3. *Lyα Escape Fraction*

We infer the escape fraction of Lyα photons ($f_{\rm esc}^{\rm Ly\alpha}$) from the Lyα and Hα luminosities. The Lyα escape fraction is an important quantity of LAEs because it can be used to probe distribution of ISM in LAEs. Since Lyα photons are resonantly scattered by neutral hydrogen (HI) gas in the ISM, $f_{\rm esc}^{\rm Ly\alpha}$ is strongly dependent on kinematics and distribution of the ISM as well as the metallicity of the ISM. For example, $f_{\rm esc}^{\rm Ly\alpha}$ will be larger if some ISM is outflowing (e.g., Kunth et al. 1998; Atek et al. 2008; Dijkstra & Wyithe 2010). Clumpy distributions of the ISM also makes $f_{\rm esc}^{\rm Ly\alpha}$ larger (e.g., Neufeld 1991; Hansen & Oh 2006; Finkelstein et al. 2008).

The Lyα escape fraction is calculated by dividing the observed Lyα luminosity by the intrinsic Lyα luminosity produced in galaxy due to star formation. To obtain $L_{\rm int}({\rm Ly\alpha})$, most studies have used SFRs derived from SED fitting or UV continuum emission. However, instantaneous SFRs from SED fitting are model-dependent and can have errors as large as two orders of magnitude (Ono et al. 2010a), and deriving SFRs from UV continua requires large correction for dust extinction. As mentioned before, the SFRs are estimated most reliably from Hα luminosities.

Recently, Hayes et al. (2010) have compared luminosity functions of LAEs and Hα emitters (HAEs) at $z = 2.2$ and found the volumetrically averaged escape fraction for star-forming galaxies to be $\sim 5\,\%$. This estimate is based on intrinsically different populations (LAEs and HAEs) and thus it is not clear whether or not LAEs typically have such low escape fractions.

We estimate $f_{\rm esc}^{\rm Ly\alpha}$ of LAEs at $z \sim 2.2$ by directly comparing the Lyα luminosity of the stacked object with its Hα luminosity. We calculate $f_{\rm esc}^{\rm Ly\alpha}$ as:

$$f_{\rm esc}^{\rm Ly\alpha} \equiv \frac{L_{\rm obs}({\rm Ly\alpha})}{L_{\rm int}({\rm Ly\alpha})} = \frac{L_{\rm obs}({\rm Ly\alpha})}{8.7 L_{\rm int}({\rm H\alpha})}, \qquad (10)$$

where subscripts ‘int’ and ‘obs’ refer to the intrinsic and observed quantities, respectively, and we assume Case B recombination (Brocklehurst 1971).

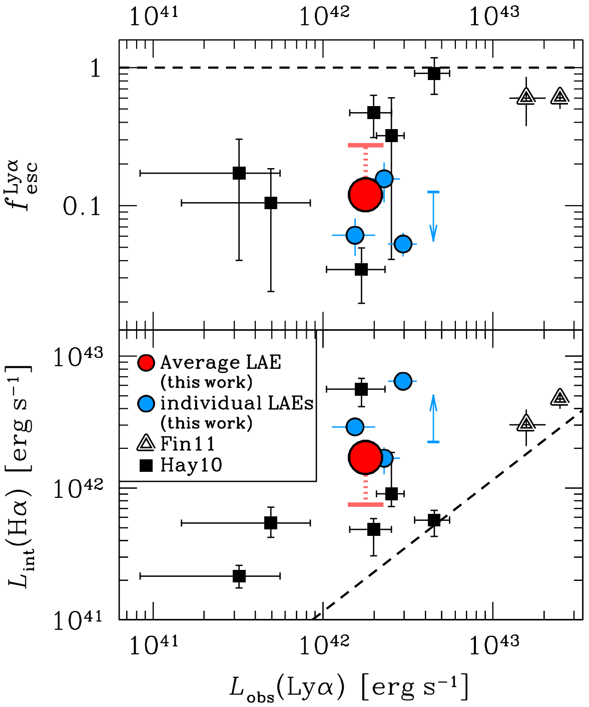

FIG. 15.— (top) Lyα escape fraction ($f_{\rm esc}^{\rm Ly\alpha}$) of LAEs against the observed Lyα luminosity. The red filled circle indicates our stacked LAE after correction for dust extinction of $E(B-V) = 0.27$, and the red horizontal bar is the case assuming $E(B-V) = 0$. The cyan circles are three individually Hα detected LAEs; for them we assume $E(B-V) = 0$, implying that their $f_{\rm esc}^{\rm Ly\alpha}$ values are upper limits; if they have $E(B-V) = 0.27$ as in the case of the stacked object, $f_{\rm esc}^{\rm Ly\alpha}$ decreases by 56 % as indicated by the cyan arrow. The filled squares show $z = 2.2$ LAEs which are also selected as Hα emitters by a double narrowband survey (Hayes et al. 2010). The open triangles denote LAEs at $z \sim 2.3$ and 2.5 whose Lyα and Hα luminosities are spectroscopically measured (Finkelstein et al. 2011). The dashed line shows $f_{\rm esc}^{\rm Ly\alpha} = 1$. (bottom) Intrinsic Hα luminosity against the observed Lyα luminosity. The meanings of the symbols and the line are the same as in the top panel.

As listed in Table 4, $L_{\rm obs}({\rm Ly\alpha})$ is $1.80^{+0.05}_{-0.07} \times 10^{42}$ erg s^{-1}. $L_{\rm int}({\rm H\alpha})$ is derived to be $1.73^{+0.28}_{-0.31} \times 10^{42}$ erg s^{-1} by correcting $L_{\rm obs}({\rm H\alpha})$ ($7.55^{+1.19}_{-1.15} \times 10^{41}$ erg s^{-1}, see Table 4) for dust extinction of $E(B-V) = 0.27^{+0.01}_{-0.03}$. From Equation (10), we find $f_{\rm esc}^{\rm Ly\alpha} = 12^{+2}_{-2}\,\%$ for the stacked object. When dust free is assumed, $f_{\rm esc}^{\rm Ly\alpha}$ can be as high as $27^{+4}_{-4}\,\%$, which is about six times higher than that derived volumetrically for star-forming galaxies at $z = 2.2$ (Hayes et al. 2010). These values suggest that for a typical LAE at $z \sim 2$ a relatively large fraction of Lyα photons can escape the galaxies. Our value is also much higher than those estimated for LBGs at $z \sim 3$ (e.g., $\sim 5\,\%$ (median); Kornei 2010), but similar to that for LAEs at $z = 2 - 3$ (29 % (median): Blanc et al. 2011, $> 32\,\%$: Hayes et al. 2010 using LAEs alone, $> 14\,\%$: Zheng et al. 2011).

It is intuitively unreasonable that galaxies with $E(B-V) = 0.27$ can escape as high as 12 % of Lyα photons. Indeed, Kornei (2010) find that $z \sim 3$ LBGs with $E(B-V) = 0.2-0.3$ have $f_{\rm esc}^{\rm Ly\alpha}$ of just a few percents. As described in §1, however, there is a possibility that dust does not always attenuate Lyα emission, but rather plays an important role in escaping Lyα photons from galaxies.

In order to quantify the effect of dust on $f_{\rm esc}^{\rm Ly\alpha}$, we introduce the parameter q following Finkelstein et al. (2008), which is defined as $q = \tau({\rm Ly\alpha})/\tau_{1216}$, where $\tau({\rm Ly\alpha})$ and τ_{1216} are defined as $e^{-\tau({\rm Ly\alpha})} = L_{\rm obs}({\rm Ly\alpha})/L_{\rm int}({\rm Ly\alpha})$ and $e^{-\tau_{1216}} = 10^{-0.4k_{1216}E(B-V)}$ with k_{1216} being the extinction coefficient at $\lambda = 1216$ Å. Small values ($q < 1$) mean that Lyα photons suffer less attenuation by dust than UV-continuum photons, as expected for a clumpy distribution of the ISM (e.g., Neufeld 1991) or special kinematics of the ISM (e.g., outflows; Kunth et al. 1998), while large values ($q > 1$) means that Lyα photons are more heavily attenuated by dust.

The q parameter is expressed in terms of $f_{\rm esc}^{\rm Ly\alpha}$ and $E(B-V)$ as:

$$q = \frac{-\log(f_{\rm esc}^{\rm Ly\alpha})}{0.4k_{1216}E(B-V)}. \tag{11}$$

Using $k_{1216} = 11.98$ (Calzetti et al. 2000) we obtain $q = 0.7^{+0.1}_{-0.1}$. Similar results have been obtained from other studies. For example, Hayes et al. (2010) obtained $q \simeq 1-1.5$ for $z = 2.2$ LAEs, and Blanc et al. (2011) found a median of $q = 0.99$ for their $z = 2-4$ LAE sample.

We note again that the $E(B-V)$ value of our stacked object estimated by SED fitting may suffer additional errors due to possible systematic uncertainties (see §5), so may the q-value. However, even when we take an extreme case of $E(B-V) = 0.1$, q increases only up to ~ 1.5, implying that very large q ($\gg 1$) are unlikely. Our result thus favors models of LAEs' ISM being outflowing, or possessing a multi-phase clumpy distribution, or both, rather than in a homogeneous, static distribution.

We also apply Equation (10) to the individually detected objects, NB387-C-22326, NB387-W-04041, and NB387-W-04492 to obtain $f_{\rm esc}^{\rm Ly\alpha} = 6^{+2}_{-2}$, 5^{+1}_{-1}, and 16^{+5}_{-5} %, respectively. These values are derived from dust uncorrected Hα luminosities, and hence are upper limits. Figure 15 shows $f_{\rm esc}^{\rm Ly\alpha}$ against the observed Lyα luminosity for our LAEs (the red circle for the stacked object and the cyan circles for the individually detected objects) together with those LAEs taken from the literature for which Hα emission is individually detected: six LAEs at $z \sim 2.2$ whose Hα luminosities are estimated from narrowband imaging (Hayes et al. 2010) and two LAEs with Hα spectra at $z \sim 2.3$ and 2.5 (Finkelstein et al. 2011). It is found that most of the LAEs with individual Hα detection have $f_{\rm esc}^{\rm Ly\alpha} \gtrsim 10$ %, with objects brighter in Lyα luminosity tending to have higher escape fractions. It is interesting that our stacked object is roughly on this trend, since LAEs with individual Hα detection should be biased toward higher Hα luminosities. It may imply that most LAEs (irrespective of Hα detection) have relatively high $f_{\rm esc}^{\rm Ly\alpha}$, at least higher than the volumetrically averaged star-forming galaxies (Hayes et al. 2010). The trend of increasing $f_{\rm esc}^{\rm Ly\alpha}$ with Lyα luminosity seems to be natural because galaxies with higher $f_{\rm esc}^{\rm Ly\alpha}$ have brighter Lyα luminosities and thus are more easily selected as LAEs. Finally, we note that recent studies have shown that a fraction of Lyα is emitted from diffuse outer halos of galaxies (e.g., Steidel et al. 2011). We estimate the strength of Lyα from the color u^*-NB387 with a certain aperture, therefore the escape fraction we derive is only the fraction escaping from the central region of the LAEs.

7. CONCLUSIONS

We have presented the results of the first detection of [O II] and Hα emission from a typical Lyα emitter (LAE) at $z = 2.2$ using a stacking analysis of a sample constructed from our Subaru/Suprime-Cam narrowband (NB387) survey in the Subaru/*XMM-Newton* Deep Survey field. The redshift $z = 2.2$ is unique, because [O II] and Hα lines fall into NIR wavelengths where OH-airglow is very weak. We found 919 LAE candidates in this field. Follow-up spectroscopy was made for 30 candidates selected to cover wide ranges of NB387 magnitudes and u^*-NB387 colors. Among the 13 out of 30 candidates with NB387 < 25, 10 were confirmed as $z \sim 2.2$ LAEs. No emission line was detected for the remaining 20 with NB387 > 25 due to the lack of sensitivity.

The near infrared observation was made to detect [O II] and Hα lines by the NewHα Survey (Lee et al. in preparation) with KPNO/NEWFIRM, using the narrowband filters NB118 and NB209, respectively; 561 LAEs are located in the area covered by NB118 (NB118 sub-sample), among which 105 have also NB209 imaging (NB209 subsample).

Only seventeen and seven candidates are individually detected in NB118 and NB209, respectively. However, a stacking analysis of a large number of undetected LAEs yielded statistically significant detection in both narrowbands. We estimated the [O II] and Hα+[N II] EWs and fluxes of the stacked object using Monte Carlo simulations, and used the estimates to derive the SFR, gas phase metallicity, and Lyα escape fraction ($f_{\rm esc}^{\rm Ly\alpha}$) of a typical LAE. Our main results probed by the triple narrow-band survey are summarized as follows.

- The Hα luminosity of the stacked object, after correction for a contribution from [N II] lines (estimated to be modest) to the Hα+[N II] photometry and for a dust extinction of $E(B-V) = 0.27^{+0.01}_{-0.03}$ (derived from SED fitting), is $1.7^{+0.3}_{-0.3} \times 10^{42}$ erg s^{-1}, which corresponds to a SFR of $14^{+2}_{-3}\,M_\odot$ yr^{-1}. This is the first estimate of the SFR of a typical LAE at high-z based on the Hα luminosity. Adopting an stellar mass of $5 \times 10^8\,M_\odot$ derived from SED fitting, we plot the stacked object on the specific SFR (sSFR) vs. $M_\star$ plane, and find that our stacked object is located below a simple extrapolation toward lower-masses of the observed sSFR - $M_\star$ relation of $z \sim 2$ BzK and UV-selected galaxies. This trend is also evident for LAEs at similar redshifts whose SFRs are inferred by SED fitting. This indicates that low-mass galaxies with $M \lesssim 10^{9-10}\,M_\odot$ have lower star formation efficiencies than expected from massive galaxies.

- We use the line ratio [O II]/(Hα+[N II]) as a metallicity indicator, and find that the metallicity of the stacked object is no less than $0.09\,Z_\odot$ at the 2σ level. This is the first constraint on the metallicity of a typical LAE at high-z, and this relatively high lower-limit does not support, at least at $z \sim 2$, the hypothesis that LAEs are extremely metal poor ($Z < 2\times10^{-2}\,Z_\odot$) galaxies at the 4σ level. We plot the stacked object on the mass-metallicity ($M-Z$)

plane, and find that the stacked object is not consistent with a simple extrapolation toward lower masses of the observed $M - Z$ relation of $z \sim 2$ UV-selected galaxies. Instead, our result seems to be consistent with the recently proposed fundamental $M - Z$ relation (Mannucci et al. 2010) for which the relatively low SFR of the stacked object is taken into account.

- From the Lyα and Hα luminosities, we found that the $f_{\rm esc}^{\rm Ly\alpha}$ of the stacked object is $12^{+2}_{-2}\,\%$, and can be as high as $27^{+4}_{-4}\,\%$, much larger than those inferred for volumetrically averaged star forming galaxies at $z = 2.2$ and Lyman-break galaxies at higher-z, but comparable to those of LAEs at $z = 2 - 3$. We compiled the $f_{\rm esc}^{\rm Ly\alpha}$ data of LAEs with Hα emission from the literature, and found that most LAEs have relatively high $f_{\rm esc}^{\rm Ly\alpha}(\gtrsim 10\,\%)$, and that there are a mild trend that brighter LAEs have higher $f_{\rm esc}^{\rm Ly\alpha}$. We also found a low q value for our object, $q = 0.7^{+0.1}_{-0.1}$. All these findings indicate that LAEs have some unique mechanisms to efficiently emit Lyα photons.

The NB387 data used in this work are collected at the Subaru Telescope, which is operated by the National Astronomical Observatory of Japan. We sincerely thank the Subaru Telescope staff for their great helps of our Suprime-Cam observations. We thank Matthew Hayes for kindly providing us Lyα and Hα data of his LAE sample as well as useful comments on escape fraction of Lyα photons. We also thank Tohru Nagao and Roberto Maiolino who gave us their emission-line flux and metallicity measurements of local galaxies as well as many fruitful comments on metallicity indicators. We thank Chris Simpson for providing the radio source catalog for the SXDS. We thank Lucia Guaita for providing us the average SED of $z \sim 2$ BX galaxy. We are grateful to Steven L. Finkelstein, Maritza Lara-Lopez, Filippo Mannucci, Kentaro Motohara, and Zhen-Ya Zheng for their helpful comments and discussions. We thank the referee for his/her lots of helpful comments and suggestions which improved this paper. This work is based in part on observations made with the Spitzer Space Telescope, which is operated by the Jet Propulsion Laboratory, California Institute of Technology under a contract with NASA. Support for this work was provided by NASA through an award issued by JPL/Caltech. This work was supported by World Premier International Research Center Initiative (WPI Initiative), MEXT, Japan.

Facilities: Subaru (Suprime-Cam), KPNO:Mayall (NEWFIRM), CFHT:MegaPrime (MegaCam), UKIRT (WFCAM), Magellan:Baade (IMACS), Spitzer (IRAC)

REFERENCES

Allende Prieto, C., Lambert, D. L., & Asplund, M. 2001, ApJ, 556, L63
Atek, H., Kunth, D., Hayes, M., Östlin, G., & Mas-Hesse, L. M. 2008, A&A, 488, 491
Bardeen, J. M., Bond, J. R., Kaiser, N., & Szalay, A. S. 1986, ApJ, 304, 15
Benson, A. J. 2010, Phys. Rep., 495, 33
Bertin, E., & Arnouts, S. 1996, A&AS, 117, 393
Blanc, G. A., et al. 2011, ApJ, 736, 31
Blumenthal, G. R., Faber, S. M., Primack, J. R. & Rees, M. J. 1984, Nature, 311, 517
Brinchmann, J., Charlot, S., White, S. D. M., Tremonti, C., Kauffmann, G., Heckman, T., & Brinkmann, J. 2004, MNRAS, 351, 1151
Brocklehurst, M. 1971, MNRAS, 153, 471
Bruzual, G., & Charlot, S. 2003, MNRAS, 344, 1000
Calzetti, D., Armus, L., Bohlin, R. C., Kinney, A. L., Koornneef, J., & Storchi-Bergmann, T. 2000, ApJ, 533, 682
Charlot, S., Kauffmann, G., Longhetti, M., Tresse, L., White, S. D. M., Maddox, S. J., & Fall, S. M. 2002, MNRAS, 330, 876
Cooper, M. C., et al. 2006, MNRAS, 370, 198
Cowie, L. L., & Hu, E. M. 1998, AJ, 115, 1319
Cowie, L. L., Barger, A. J., & Hu, E. M. 2011, ApJ, 738, 136
Daddi, E., et al. 2004, ApJ, 617, 746
Davis, M., Efstathiou, G., Frenk, C. S., & White, S. D. M. 1985, ApJ, 292, 371
Dijkstra, M., & Wyithe J. S. W. 2010, MNRAS, 408, 352
Dressler, A., Hare, T., Bigelow, B. C., & Osip, D. J. 2006, SPIE, 6269, 13
Ellison, S. L., Patton, D. R., Simard, L., & McConnachie, A. W. 2008, AJ, 135, 1877
Erb, D. K., Shapley, A. E., Pettini, M., Steidel, C. C., Reddy, N. A., & Adelberger, K. L. 2006a, ApJ, 644, 813
Erb, D. K., Steidel, C. C., Shapley, A. E., Pettini, M., Reddy, N. A., & Adelberger, K. L. 2006b, ApJ, 647, 128
Erb, D. K., Pettini, M., Shapley, A. E., Steidel, C. C., Law, D. R., & Reddy, N. A. 2010, ApJ, 719, 1168
Furusawa, H., et al. 2008, ApJS, 176, 1
Finkelstein, S. L., Rhoads, J. E., Malhotra, S., Pirzkal, N., & Wang, J. 2007, ApJ, 660, 1023
Finkelstein, S. L., Rhoads, J. E., Malhotra, S., Grogin, N., & Wang, J. 2008, ApJ, 678, 655
Finkelstein, S. L., Rhoads, J. E., Malhotra, S., & Grogin, N. 2009, ApJ, 691, 465
Finkelstein, S. L., et al. 2011, ApJ, 729, 140
Gallagher, J. S., Hunter, D. A., & Bushouse, H. 1989, AJ, 97, 700
Gawiser, E., et al. 2006, ApJ, 642, L13
Gawiser, E., et al. 2007, ApJ, 671, 278
Gilbank, D. G., Baldry, I. K., Balogh, M. L., Glasebrock, K., & Bower, R. G. 2010, MNRAS, 405, 2594
Gronwall, C., et al. 2007, ApJ, 667, 79
Guaita, L., et al. 2010, ApJ, 714, 255
Guaita, L., et al. 2011, ApJ, 733, 114
Gunn, J. E., & Stryker, L. L. 1983, ApJS, 52, 121
Hainline, K. N., Sharpley, A. E., Kornei, K. A., Pettini, M., Buckley-Geer, E., Allam, S. S., & Tucker, D. L. 2009, ApJ, 701, 52
Hansen, M., & Oh, S. P. 2006, MNRAS, 367, 979
Hayashi, M., et al. 2009, ApJ, 691, 140
Hayes, M., et al. 2010, Nature, 464, 562
Hopkins, A. M. 2004, ApJ, 615, 209
Iwata, I., et al. 2009, ApJ, 692, 1287
Jansen, R. A., Franx, M., & Fabricant, D. 2001, ApJ, 551, 825
Kashikawa, N., et al. 2006, ApJ, 648, 7
Kennicutt, R. C., Jr. 1992, ApJ, 388, 310
Kennicutt, R. C., Jr. 1998, ARA&A, 36, 189
Kewley, L. J., & Dopita, M. A. 2002, ApJS, 142, 35
Kewley, L. J., Geller, M. J., & Jansen, R. A. 2004, AJ, 127, 2002
Kewley, L. J., & Ellison, S. L. 2008, ApJ, 681, 1183
Kornei, K. A., Shapley, A. E., Erb, D. K., Steidel, C. C., Reddy, N. A., Pettini, M., & Bogosavljevic, M. 2010, ApJ, 711, 693
Kunth, D., Mas-Hesse, J. M., Terlevich, E., Terlevich, R., Lequeux, J., & Fall, S. M. 1998, A&A, 334, 11
Lai, K., et al. 2008, ApJ, 674, 70
Lala-Lopez, M. A., et al. 2010, A&A, 521, L53
Lawrence, A., et al. 2007, MNRAS, 379, 1599
Lee, J. C., Salzer, J. J., & Melbourne, J. 2004, ApJ, 616, 752
Ly, C., et al. 2011, ApJ, 726, 109
Madau, P. 1995, ApJ, 441, 18
Maiolino, R., et al. 2008, A&A, 488, 463

Malhotra, S., & Rhoads, J. E. 2002, ApJ, 565, 71
Malhotra, S., & Rhoads, J. E. 2004, ApJ, 617, 5
Mannucci, F., et al. 2009, MNRAS, 398, 1915
Mannucci, F., Cresci, G., Maiolino, R., Marconi, A., & Gnerucci, A. 2010, MNRAS, 408, 2115
Mannucci, F., Salvaterra, R., & Campisi, M.A. 2011, MNRAS, 414, 1263
McLinden, E. M., et al. 2011, ApJ, 730, 136
Miyazaki, S., et al. 2002, PASJ, 54, 833
Moustakas, J., Kennicutt, R. C., Jr., & Tremonti, C. A. 2006, ApJ, 642, 775
Nagao, T., Maiolino, R., & Marconi, A. 2006, A&A, 459, 85
Nestor, D. B., Shapley, A. E., Steidel, C. C., & Siana, B. 2011, ApJ, 736, 18
Neufeld, D. A. 1991, ApJ, 370, L85
Nilsson, K. K., et al. 2007, A&A, 471, 71
Nilsson, K. K., et al. 2009, A&A, 498, 13
Nilsson, K. K., Östlin, G., Møller, P.,Möller-Nilsson, O., Tapken, C., Freudling, W., & Fynbo, J. P. U. 2011, A&A, 529, 9
Oke, J. B. 1974, ApJS, 27, 21
Oke, J. B. 1990, AJ, 99, 1621
Ono, Y., et al. 2010a, MNRAS, 402, 1580
Ono, Y., Ouchi, M., Shimasaku, K., Dunlop, J., Farrah, D., McLure, R., & Okamura, S. 2010b, ApJ, 724, 1524
Osterbrock, D. E. 1989, Astrophysics of Gaseous Nebulae and Active Galactic Nuclei. University Science Books, Suasalito, CA
Ouchi, M., et al. 2003, ApJ, 582, 60
Ouchi, M., et al. 2004, ApJ, 611, 660
Ouchi, M., et al. 2008, ApJS, 176, 301
Ouchi, M., et al. 2010, ApJ, 723, 869
Pettini, M., et al. 2001, ApJ, 554, 981
Pettini, M., & Pagel, B. E. J. 2004, MNRAS, 348, 59
Pirzkal, N., Malhotra, S., Rhoads, J. E., & Xu, C. 2007, ApJ, 667, 49
Polletta, M., et al. 2007, ApJ, 663, 81
Reddy, N. A., et al. 2006, ApJ, 644, 792
Richard, J., Jones, T., Ellis, R., Stark, D. P., Livermore, R., & Swinbank, M. 2011, MNRAS, 413, 643
Rigby, J. R., Wuyts, E., Gladders, M. D., Sharon, K., & Becker, G. D. 2011, ApJ, 732, 59
Salpeter, E. E. 1955, ApJ, 121, 161
Scannapieco, E., Schneider, R., & Ferrara, A. 2003, ApJ, 589, 35
Schlegel, D. J., Finkbeiner, D. P., & Davis, M. 1998, ApJ, 500, 525
Schaerer, D. 2003, A&A, 397, 527
Schaerer, D. & de Barros, S. 2009, A&A, 502, 423
Shimasaku, K., et al. 2006, PASJ, 58, 313
Simpson, C., et al. 2006, MNRAS, 372, 741
Steidel, C. C., & Hamilton, D. 1992, AJ, 104, 941
Steidel, C. C., et al. 2010, ApJ, 717, 289
Steidel, C. C., Bogosavljevic, M., Shapley, A. E., Kollmeier, J. A., Reddy, N. A., Erb, D. K., Pettini, M. 2011, ApJ, 736, 160
Takahashi, M. I., et al. 2007, ApJS, 172, 456
Tanaka, I., et al. 2011, PASJ, 63, 415
Teplitz, H. I., Collins, N. R., Gardner, J. P., Hill, R. S., & Rhodes, J. 2003, ApJ, 589, 704
Tremonti, C. A., Heckman, T. M., Kauffmann, G., et al. 2004, ApJ, 613, 898
Tresse, L., Maddox, S. J., Le Fèvre, O., & Cuby, J. -G. 2002, MNRAS, 337, 369
Ueda, Y., et al. 2008, ApJS, 179, 124
van Dokkum, P. G. 2001, PASP, 113, 1420
Yagi, M., Kashikawa, N., Sekiguchi, M., Doi, M., Yasuda, N., Shimasaku, K., & Okamura, S. 2002, AJ, 123, 66
Yoshikawa, T., et al. 2010, ApJ, 718, 112
Yuma, S., et al. 2010, ApJ, 720, 1016
Zheng, Z. Y., et al. 2011, ArXiv e-prints, 1011, arXiv:1106.2811